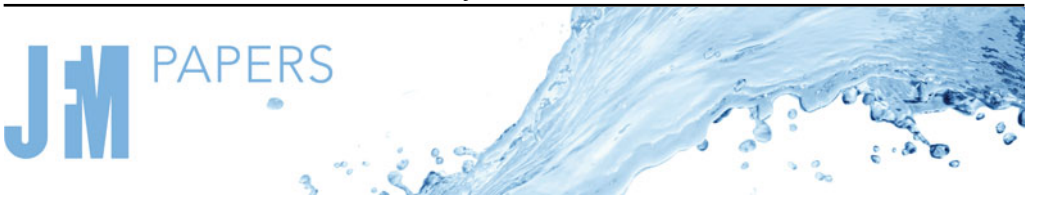
J. Fluid Mech. (2025), *vol.* 1021, A18, doi:10.1017/jfm.2025.10708



On the receptivity of first and cross-flow modes in hypersonic sharp wing flows

Jiachen Lu[1], **Ken Chun Kit Uy**[1], **Rui Zhao**[2] **and Chihyung Wen**[1]

[1]Department of Aeronautical and Aviation Engineering, The Hong Kong Polytechnic University, Hung Hom, Kowloon, Hong Kong SAR, PR China

[2]School of Aerospace Engineering, Beijing Institute of Technology, Beijing, 100081, PR China

Corresponding author: Rui Zhao, zr@bit.edu.cn

(Received 18 March 2025; revised 15 July 2025; accepted 12 September 2025)

A long-standing conceptual debate regarding the identification and independence of first Mack and cross-flow instabilities is clarified over a Mach 5.9 sharp wing at zero angle of attack and varying sweep angles. Their receptivity of the boundary layers to three-dimensional slow acoustic and vorticity waves is investigated using linear stability theory, direct numerical simulation and momentum potential theory (MPT). Linear stability theory demonstrates that the targeted slow mode appears as the oblique first mode at small sweep angles (0° and 15°) and transitions to the cross-flow mode at larger sweep angles (30° and 45°). Direct numerical simulation indicates that both the oblique first mode and cross-flow mode share identical receptivity pathways: for slow acoustic waves, the pathway comprises 'leading-edge damping–enhanced exponential growth–linear growth' stages. For vorticity waves, it consists of 'leading-edge damping–non-modal growth–linear growth' stages. Momentum potential theory decomposes the fluctuation momentum density into vortical, acoustic and thermal components, revealing unified receptivity mechanisms: for slow acoustic waves, the leading-edge damping is caused by strong acoustic components generated through synchronization. The enhanced exponential growth stage is dominated by steadily growing vortical components, with acoustic and thermal components remaining at small amplitudes. For vorticity waves, leading-edge disturbances primarily consist of vortical components, indicating a distinct mechanism from slow acoustic waves. Non-modal stages originate from adjustments among MPT components. Vortical components dominate the linear growth stage for both instabilities. These uniform behaviours between first Mack and cross-flow modes highlight their consistency.

Key words: boundary layer receptivity, hypersonic flow, boundary layer stability

© The Author(s), 2025. Published by Cambridge University Press.

https://doi.org/10.1017/jfm.2025.10708 Published online by Cambridge University Press

1. Introduction

The laminar–turbulent transition in hypersonic boundary layers represents a critical consideration for high-speed vehicle design, primarily due to its substantial amplification of localized thermal loads. In low-disturbance flight environments, this transition process follows these fundamental stages (Morkovin, Reshotko & Herbert 1994; Fedorov 2011): (i) receptivity; (ii) linear instability; (iii) nonlinear instability; (iv) breakdown. During the receptivity phase, external free stream perturbations, such as acoustic waves, entropy fluctuations or vortical disturbances, interact with the boundary layer, generating instability modes within the shear layer (Saric, Reed & Kerschen 2002; Balakumar 2015). The initial amplitudes of unstable modes typically remain orders of magnitude below characteristic flow scales, permitting linear stability theory (LST) to accurately model the exponential growth of instabilities during the linear stage. Farther downstream, the amplitudes of the disturbances eventually saturate, nonlinear interactions and secondary instabilities emerge, and the flow undergoes rapid breakdown to turbulence within a brief downstream interval.

Linear stability theory enables detailed analysis of linear instability mechanisms, with several instabilities identified as primary drivers of transition in supersonic flows (Mack 1975; Malik 1990; Liu 2022), including the first Mack mode, the second Mack mode and the cross-flow mode. Along quasi-two-dimensional (quasi-2-D) supersonic aircraft leading edges, the first mode is the most amplified instability at low-Mach-number boundary layers, whereas the second mode exhibits higher growth rates as the Mach number exceeds 3.8 (Mack 1984; Malmuth *et al.* 1998; Fedorov 2011). In the three-dimensional (3-D) boundary layers subject to pressure gradients and sweep effects, curved inviscid streamlines at the boundary layer edges induce an inflection point within the cross-flow profile (Saric, Reed & White 2003). The cross-flow instability, known as another strong modal instability, originates from this inflection point and serves as a prevalent and important mechanism in the transition stage among various 3-D configurations, such as yawed cones (Li *et al.* 2010; Craig & Saric 2016; Moyes *et al.* 2016; Chen *et al.* 2021*b*), swept wings (Xu *et al.* 2019; Chen *et al.* 2021*a*; Qiu *et al.* 2024) and other complex configurations (Fezer & Kloker 2003; Wassermann & Kloker 2005; Balakumar & King 2012; Wheaton *et al.* 2021; Chen *et al.* 2022; Quintanilha *et al.* 2022).

Previous research on hypersonic boundary-layer instability has predominantly focused on second Mack modes due to their characteristically high growth rates (Reed, Saric & Arnal 1996; Fedorov 2011). The receptivity stage of second Mack modes, establishing the initial disturbance amplitudes of instabilities, has also been thoroughly investigated (Fedorov 2002; Chen *et al.* 2021*c*; Wan *et al.* 2022; Niu & Su 2023).Fedorov & Khokhlov (2001) pioneered this field by establishing a theoretical framework via the multiple-mode method, demonstrating that second Mack modes arise from the excitation of the fast (F) or slow (S) mode near the leading-edge and intermodal conversion downstream at the synchronization point, where F- and S-modes share nearly identical phase speeds. Subsequently, Ma and Zhong conducted a series of numerical simulations on the receptivity of a Mach 4.5 sharp flat plate boundary layer to acoustic, vortical and entropy waves (Ma & Zhong 2003*a*;2003*b*; 2005), which physically relate to pressure, temperature (or density) and velocity fluctuations (Zhong & Wang 2012). Their results further affirm the synchronization theory of Fedorov and Khokhlov. Balakumar *et al.*, numerically investigated the boundary-layer receptivity over diverse geometries, e.g. sharp and blunt cones (Kara, Balakumar & Kandil 2011), straight and flared cones (Balakumar & Kegerise 2015), sharp and blunt wedges (Balakumar 2015), further confirming Fedorov's synchronization theory when the disturbance frequency supports the second mode.

https://doi.org/10.1017/jfm.2025.10708 Published online by Cambridge University Press

Although second Mack modes typically exhibit higher growth rates, several experimental and numerical results highlight that the low-frequency disturbances, i.e. the first Mack mode and the cross-flow mode, are also essential for boundary layer transition. Fezer & Kloker (2003) compared transition mechanisms over a flat plate and a sharp cone at Mach 6.8. Oblique breakdown induced by 3-D first modes is expected to be the dominant transition mechanism for the flat plate. Chen, Zhu & Lee (2017) examined the transition process of a hypersonic boundary layer on a flared cone and found that low-frequency disturbances are heavily amplified via parametric resonance despite the second mode possessing a much higher localized growth rate. Zhu *et al.* (2021) further discovered that soliton-like wave packets, which play a determining role in turbulence production, originate from the vortical first Mack mode rather than the rapidly growing dilatational second Mack mode. Recently, Guo, Hao & Wen (2023) analysed the nonlinear interaction and breakdown process of a Mach 6 flat-plate boundary layer. The results indicate that the integrated Chu's energy of the oblique first mode is comparable to that of the planar second mode, even though the growth rate of the second mode surpasses that of the oblique wave. The oblique first mode is a key source of a detuned mode, critical to breakdown. For instance, Wan *et al.* (2021) conducted a hypersonic model flight experiment of an inclined blunt cone, revealing that low-frequency pressure signals, peaking at approximately 10 kHz and identified as travelling cross-flow modes, are pivotal in the transition process. Travelling cross-flow instability can also play a dominant role in transition when travelling cross-flow vortices and second modes coexist within the boundary layer. According to Qiu *et al.* (2024), travelling cross-flow vortices are essential for forming low-frequency hairpin-like structures that ultimately trigger turbulence.

The importance of first and cross-flow modes has been highlighted by these studies. Quantifying their initial amplitudes is of great importance for engineering. In subsonic flows, receptivity mechanisms have been established experimentally. Saric *et al.* (2002) reviewed experimental studies on subsonic 2-D flat-plate boundary layers, demonstrating that vortical waves contribute to the 3-D aspects of the breakdown process, whereas acoustic disturbances excite the initial amplitudes of the 2-D Tollmien–Schlichting (TS) waves. Deyhle & Bippes (1996) found that stationary cross-flow modes, triggered by surface roughness, prevail under low turbulence levels. Travelling cross-flow modes exhibit receptivity to vorticity but not to acoustic disturbances. In supersonic and hypersonic regimes, the receptivity mechanism of cross-flow modes becomes more complex (Su & Geng (2017)). Some supersonic experiments report travelling cross-flow mode dominance even with weak free stream disturbances (Owens *et al.* 2014; Niu *et al.* 2019; Wan *et al.* 2021). Craig & Saric (2016) observed coexistences of stationary and travelling cross-flow modes, arguing that this behaviour remains in partial agreement with the low-speed case. Niu *et al.* (2020, 2021, 2024) observed travelling cross-flow modes across several configurations in a noisy wind tunnel, showing that travelling cross-flow instabilities are dominant under high turbulence levels. Experiments inherently contain various types of disturbances, complicating the analysis of receptivity mechanisms. Theoretical and numerical analyses are essential to clarify these mechanisms. However, despite extensive investigations of second Mack modes, theoretical and numerical research on the receptivity of first and cross-flow modes to free stream disturbances remains limited. When the frequency is not high enough to sustain the second mode, the F-mode remains neutral within the boundary layer, precluding synchronizations between the F-mode and vortical or S-modes (Fedorov & Tumin 2011). This results in fundamentally divergent receptivity pathways compared with second Mack modes. Balakumar & King (2011) quantified the receptivity of a Mach 3 swept wing boundary layer with direct numerical simulation (DNS), proposing receptivity coefficients for roughness, acoustic and vortical

https://doi.org/10.1017/jfm.2025.10708 Published online by Cambridge University Press

disturbances. Their results demonstrated that acoustic disturbances are approximately eight times weaker in generating unstable travelling cross-flow vortices compared with the vorticity waves. Xu *et al.* (2018) applied LST in a Mach 6, 3-D boundary layer, showing that the discrete-spectrum slow mode can be excited by the slow acoustic waves from the continuous spectrum near the leading edge, and evolve downstream into the unstable travelling cross-flow mode. Liu, Dong & Wu (2020) combined triple-deck theory and DNS to reveal a pathway of generating first Mack modes through the interaction between slow acoustic waves and streamwise isolated wall roughness.

A long-standing conceptual debate in hypersonic regimes concerns the independence and identification of the first Mack and cross-flow modes. In low Mach number regimes, the cross-flow instability and the TS wave (or the first Mack mode) occupy distinct frequency ranges (Wassermann & Kloker 2005; Liu 2022; Song & Dong 2023). In particular, Wassermann & Kloker (2005) show that cross-flow mode is asymmetric whereas TS mode is symmetric on the LST diagram for an incompressible 3-D boundary layer flow in the local streamline-oriented system, enabling a clear distinction between those modes. Liu (2022, 2023) employed the compressible Falkner–Skan–Cooke flow model and LST to investigate the theoretical property of first and cross-flow instabilities. Interestingly, these two modes appear to be distinguishable when the local stability analysis is restricted to specific limits: in the zero-frequency limit, the cross-flow mode is active while the TS mode is absent; conversely, in the zero-spanwise-wavenumber limit, the TS mode dominates and the cross-flow mode vanishes. However, when both frequency and spanwise wavenumber are considered simultaneously at Mach numbers greater than 1.5, these modes become indistinguishable, merging into a single instability mode with a single peak in the LST growth rate contours (see, e.g. Liu 2022, figure 12). A similar merging behaviour was reported by Song & Dong (2023) for the modified Mack and cross-flow modes in the boundary layer over a rotating cone at Mach 3. The same identification challenges were observed by Peck, Groot & Reed (2024) in a study of a highly swept fin positioned over a cone at a Mach number of 6. In that configuration, the flow between the transition front and the fin leading edge is subject to large cross-flow velocities and strong pressure gradients. However, their energy budget analysis indicated that the magnitudes of cross-flow-related terms were not substantial compared with streamwise terms. Whether the primary mechanism for transition is driven by cross-flow instability or the first Mack mode remains uncertain. Several criteria attempt to determine whether the dominant instability in transition is the first Mack mode or the cross-flow mode. Reed & Saric (1989) proposed a threshold for low-speed scenarios where transition is attributed to the cross-flow mode if the maximum cross-flow velocity exceeds 3 % of the boundary-layer-edge velocity. Liu (2023) suggested that the $|u'|$ profile of TS modes (or first modes) exhibits dual peaks in the weakly compressible regime, versus cross-flow modes display a single peak. However, both metrics can be problematic in high-speed regimes and geometrically complex flows with distorted boundary layers (e.g. Peck *et al.* 2024). To date, distinguishing these two modes still relies on the classical understanding dating from two decades ago: the emergence of zero-frequency instability (Wassermann & Kloker 2005) and pressure gradient responses, where favourable pressure gradients damp first modes (Zurigat, Nayfeh & Masad 1992; Masad & Zurigat 1994) but amplify cross-flow instabilities (Saric & Reed 2003).

Fundamental questions persist regarding the mode identification, particularly given their S-mode identity, overlapping frequency responses and analogous sensitivities to Mach number and wall thermal conditions. This raises intriguing questions: Are they actually the same instability? Do the consistent responses originate from their same nature? Further, are the traditional terminologies, ‘first Mack mode’ and ‘cross-flow mode’,

https://doi.org/10.1017/jfm.2025.10708 Published online by Cambridge University Press

still appropriate for characterizing hypersonic S-modes? The present paper aims to introduce a new perspective on these debates by examining the receptivity process of first and cross-flow modes. As the receptivity stage explains the origins of instabilities, divergent receptivity pathways would imply independent instability mechanisms. Clarifying whether these modes share identical receptivity pathways provides new evidence for the controversy.

This investigation presents a comprehensive analysis of receptivity mechanisms in hypersonic sharp-wing boundary layers. The sweep angle will be varied to examine the response of the hypersonic boundary layers to free stream slow acoustic and vortical waves. Several techniques will be employed: LST evaluates boundary-layer instability characteristics; DNS resolves the receptivity process and obtains the perturbation field; momentum potential theory (MPT) provides a physics-based analysis of the receptivity process. Momentum potential theory decomposes the momentum density field $\rho \boldsymbol{u}$ as $\boldsymbol{u}$ refers to the velocity vector into vortical, acoustic and thermal components (Doak 1989, 1998). Recent advancements have demonstrated that MPT can provide an intuitive and systematic interpretation for the evolution and damping of unstable modes (Unnikrishnan & Gaitonde 2019; Long *et al.* 2021; Zhu & Lee 2022; Lu *et al.* 2025). The MPT framework is employed to analyse the 3-D receptivity process for the first time. This work proposes a different approach for clarifying the origin of first and cross-flow modes, potentially introducing a new framework for resolving modal identification challenges.

The rest of the paper is organized as follows. Section 2 establishes the problem formulation and baseflow characteristics for the hypersonic spanwise-infinite swept wing configuration. Section 3 presents LST results, identifying dominant instability mechanisms. In § 4, receptivity processes of spanwise-infinite swept wing flows are simulated via DNS, subsequently elucidating receptivity pathways. A physics-based interpretation of the receptivity pathway is established with MPT. Section 5 concludes the study.

2. Problem description and baseflow property

This investigation specifically examines the first Mack mode and cross-flow instabilities over a spanwise-infinite swept wing at zero angle of attack, as illustrated in figure 1. Here x, y and z represent the Cartesian coordinates, and s, η and z denote the local body-fitted coordinates, Λ is the sweep angle, U_∞ is the free stream velocity. Figure 1*(b)* illustrates the top view of the wing. Here k_∞ is the free stream wavevector in the $x-z$ plane. It should be noted that the wave angle θ_∞ is defined between the wavevector k_∞ and the free stream velocity U_∞ to facilitate further calculations. The blue line represents an inviscid streamline, with the streamline-aligned velocity u_s and the cross-flow velocity u_c marked with yellow arrows. As depicted in figure 1(*c*), the geometry of the biconvex airfoil is an arc, designed to sustain quasiconstant pressure gradients, with a chord length of 200 and a thickness of 1, where the length scales are non-dimensionalized by a reference length $L^* = 0.001$ m. The 1 : 200 thickness-to-chord ratio ensures moderate pressure gradient ranges, as the first Mack modes are fully damped under large favourable pressure gradients. This small thickness also results in relatively small discrepancies between x and s. The baseflow for a wing with a thickness of 0.5 is also simulated using identical numerical methods for LST analysis. Figure 1(*d*) illustrates the grid and boundary conditions for DNS. The DNS framework achieves resolution fidelity via very dense grids $1281 \times 501 \times 21$ ($x \times y \times z$). The grid can be divided into three parts: the first part ranging from $x = -4$ to 40 (red region marked in figure 1*d*) includes 881 x direction grid points to promise a very high grid resolution near the leading edge ensuring that the interactions between the boundary

https://doi.org/10.1017/jfm.2025.10708 Published online by Cambridge University Press

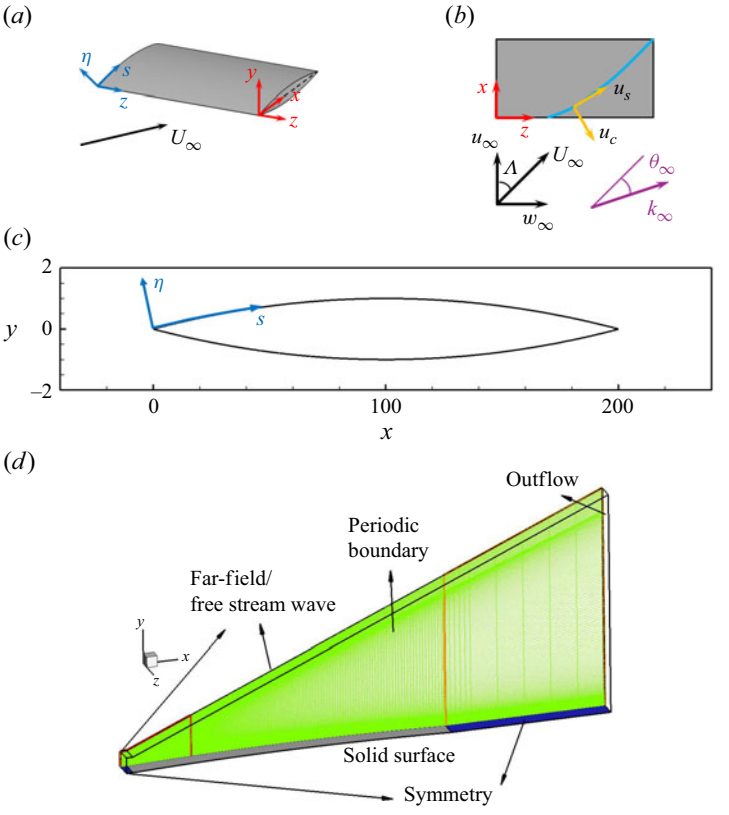


Figure 1. The schematic of the spanwise-infinite swept wing and coordinate systems: (*a*) the overall view, (*b*) the top view, (*c*) the side view, (*d*) the grid and boundary conditions; every two points are shown in the x and y directions.

layer and free stream waves are captured exactly. This grid resolution promises at least 101 grid points for one wavelength in x direction (for the vorticity wave case at $\Lambda = 45°$) and 21 grid points for one wavelength in z direction. The second part, ranging from $x = 40$ to 200, employs a medium grid resolution ($381 \times 501 \times 21$) to establish a proper background baseflow field. The third part is the sponge region ranging from $x = 200$ to 300 (orange region marked in figure 1*d*), only employing a very coarse grid ($21 \times 501 \times 21$). Grid independence is validated in the Appendix. The boundary conditions utilized in this study are shown in figure 1(*d*). At the inlet and upper surface, supersonic far-field boundary conditions are used for baseflow calculation, and free stream waves are superposed for receptivity calculation. Periodic conditions and supersonic outlet boundary conditions (with a coarse sponge layer) are used for the two lateral boundaries and the outlet of the domain, respectively. The lower surface before and after the wing surface ($x < 0$ and >200) are symmetry conditions. The wing surface is set to be a non-slip adiabatic wall.

The free stream conditions align with the experiment set-up of Stetson (1983), which are summarized in table 1. The sweep angle Λ ranges from 0° to 45°, enabling a systematic analysis of receptivity mechanism evolution across the first Mack mode and cross-flow instabilities.

https://doi.org/10.1017/jfm.2025.10708 Published online by Cambridge University Press

Ma	$Re^*_\infty(\mathrm{m}^{-1})$	$T^*_\infty(\mathrm{K})$	$\Lambda(^\circ)$
5.9	9.15×10^7	76.74	0, 15, 30, 45

Table 1. Free stream conditions.

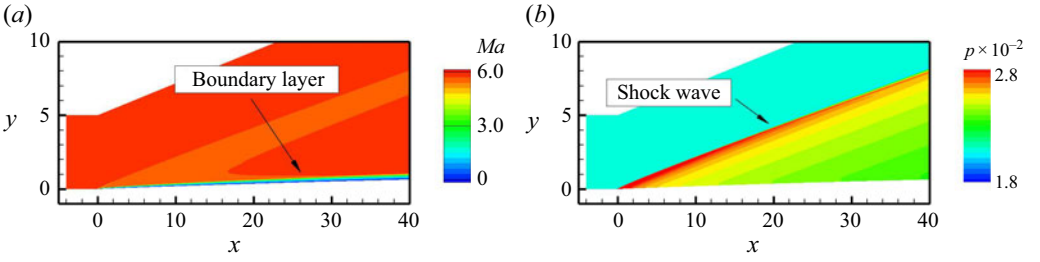


Figure 2. (*a*) The Mach number contour and (*b*) the pressure contour over the front airfoil ($0 \leqslant x \leqslant 40$) for the $\Lambda = 0^\circ$ case.

The governing equations for the DNS are the 3-D compressible Navier–Stokes equations, which can be written in the conservative form as

$$\frac{\partial}{\partial t}\boldsymbol{Q}_i + \frac{\partial}{\partial x_j}\left(\boldsymbol{F}_{ij} - \boldsymbol{F}_{v\cdot ij}\right) = 0 \tag{2.1}$$

where t and x_j are time and the Cartesian coordinates, $\boldsymbol{Q}$ is the vector of conservative variables, $\boldsymbol{F}$ and $\boldsymbol{F}_v$ are inviscid and viscous flux vectors. The governing equations are closed by the equation of state of an ideal gas. The Prandtl number $Pr = 0.72$ and the ratio of specific heats $\gamma = 1.4$. Sutherland's law is used to obtain the dynamic viscosity μ (Hao *et al.* 2022; Guo, Hao & Wen 2025; Huang *et al.* 2025). Spatial discretization applies the fifth-order upwind scheme for inviscid fluxes and the second-order central differencing scheme for viscous terms. The lower–upper symmetric Gauss–Seidel scheme is employed to resolve the steady flow field, and a third-order total variation diminishing Runge–Kutta scheme is used for unsteady temporal integration. This DNS code has been used to study the instabilities in hypersonic boundary layers in our previous research (Zhao *et al.* 2018, 2019; Liu *et al.* 2023), and more detailed validations can be found in Lu *et al.* (2025). The calculation process is stated as follows: the maximum residual reaches a small value of the order of 10^{-18} for the steady baseflow; then the unsteady free stream disturbances are superposed at the inlet and upper surface for simulating the leading-edge receptivity process. The detailed formations of the unsteady simulation and free stream waves are summarized in § 4.

In this paper, dimensional flow variables are non-dimensionalized by the steady-state free stream conditions. Specifically, length scales are non-dimensionalized by a reference length $L^* = 0.001$ m, time scales by L^*/U^*_∞. The density, velocity, temperature and pressure are made dimensionless by the free stream parameters ρ^*_∞, U^*_∞, T^*_∞ and $\rho^*_\infty U^{*2}_\infty$. In the current study, the asterisk superscript '$*$' typically signifies dimensional variables, whereas symbols without subscript '$*$' represent non-dimensional variables.

Mach number distributions and pressure contours over the front airfoil ($0 \leqslant x \leqslant 40$) for the $\Lambda = 0^\circ$ case are displayed in figure 2. A weak shock forms at the leading edge of the airfoil, followed by progressive pressure reduction through surface-generated expansion waves. Away from near-wall regions, Mach numbers exceed 5, maintaining hypersonic

https://doi.org/10.1017/jfm.2025.10708 Published online by Cambridge University Press

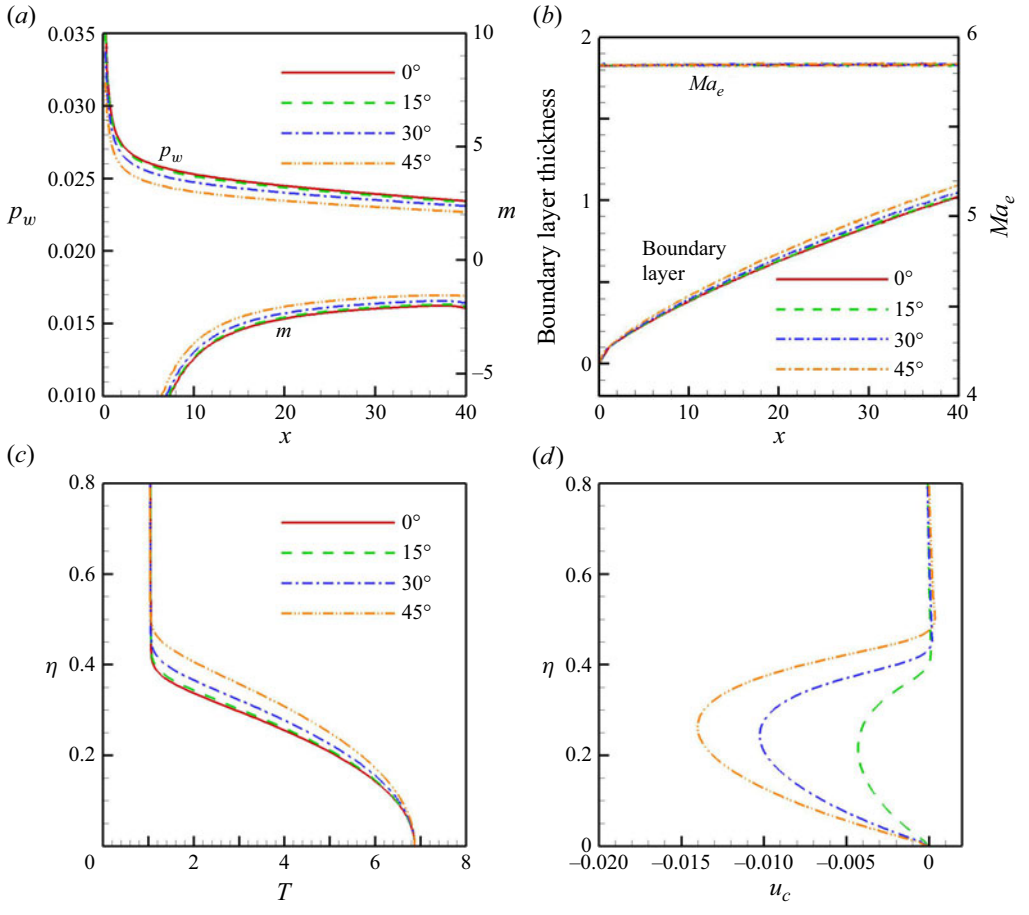


Figure 3. (*a*) Pressure and pressure gradients at the solid wall under different sweep angles; (*b*) boundary layer thickness and boundary layer edge Mach number under different sweep angles; (*c*) T profiles at $x = 40$; (*d*) u_c profiles at $x = 40$ in swept cases.

boundary layer conditions. Both first Mack mode and cross-flow instabilities are examined within the hypersonic regime. Figure 3(*a*) details wall pressure p_w and streamwise pressure gradient m distributions, where pressure gradient m is calculated by

$$m = \frac{1}{p_w}\frac{\mathrm{d}p_w}{\mathrm{d}s}. \tag{2.2}$$

Based on this definition, negative m values denote favourable pressure gradients. As shown in figure 3(*a*), the pressure exhibits a localized shift at the leading edge due to the shock wave, followed by a steady downstream decrease attributed to constant curvatures of the thin-wing configuration, with m achieving near-constant values. Figure 3(*b*) depicts boundary layer thickness identified by the $0.99U_\infty$ criteria and boundary layer edge Mach number Ma_e. The boundary layer thickness slightly increases as the sweep angle increases. Figure 3(*c*) depicts temperature profiles at $x = 40$. The cross-flow velocity u_c, defined as the velocity component perpendicular to the inviscid streamline, constitutes a fundamental component of cross-flow instabilities (Lekoudis 1980; Su, Li & Han 2024). Figure 3(*d*) depicts cross-flow velocity profiles across all swept cases. Elevated sweep angles induce higher cross-flow velocities, suggesting that the cross-flow instability is more likely to

https://doi.org/10.1017/jfm.2025.10708 Published online by Cambridge University Press

dominate the transition process with increasing sweep angles. The maximum cross-flow velocity is 1.5 % of the free stream velocity. This low magnitude is attributed to the deliberately small thickness and weak chordwise pressure gradient. These cross-flow velocities fall below the threshold criterion established by Reed & Saric (1989). As their criterion was derived for low-speed flows, it is not applicable to the current configuration. The subsequent LST results will further confirm the existence of cross-flow instability.

3. Linear stability theory

Spatial LST is employed to capture the unsteady modes in this hypersonic flow. The vector $\boldsymbol{Q}$ from (2.1) is decomposed into a one-dimensional steady solution and an unsteady perturbation under the parallel flow assumption. After linearization, the perturbation term in normal-model form is written as follows:

$$\boldsymbol{Q}'(s,\eta,z,t)=\widehat{\boldsymbol{Q}}(\eta)\ \exp(i(\alpha_r+\alpha_i)s+i\beta z-i\omega t). \tag{3.1}$$

Here α_r denotes the streamwise wavenumber, α_i denotes the spatial growth rate, β is the spanwise wavenumber, ω is the circular frequency.

For the current research, the Reynolds number is large, and the boundary layer thickness is much smaller than the radius of curvature. The LST incorporating local curvature effects κ is utilized for spatial analysis. The Lamé coefficients are $h_1=1+\kappa\eta$ and $h_2=h_3=1$. For this configuration, omitting curvature terms introduces less than 2 % error in growth rates. Although the correction only yields a small difference on the LST result, curvature terms are retained for theoretical rigour and precise results. An eigenvalue problem is formulated by substituting (3.1) into the linearized compressible Navier–Stokes equations with $\boldsymbol{Q}$,

$$\bar{A}\,\widehat{\boldsymbol{Q}}=(\alpha_r+i\alpha_i)\,\widehat{\boldsymbol{Q}}, \tag{3.2}$$

where $\bar{A}$ represents the Jacobian matrix composed of the inviscid and viscous fluxes and is expressed in terms of base flow quantities. The detailed formulations can be found in prior studies (Ren & Fu 2013; Song, Zhao & Huang 2020). The LST code in this study has been fully validated in our previous investigations (Uy *et al.* 2023*a*, 2023*b*; Lu *et al.* 2025).

The spatial wavenumbers α_r and β, and the spatial growth rate α_i are normalized by L^*, while the circular frequency ω is normalized by U_∞^*/L^*. The transformation between dimensionless circular frequency (ω) and dimensional frequency (F^*), dimensionless spanwise wavenumber (β) and dimensional spanwise wavelength (λ_z^*) are

$$\omega=\frac{2\pi\times F^*\times L^*}{|U_\infty^*|}\quad \beta=\frac{2\pi\times L^*}{\lambda_z^*}. \tag{3.3}$$

The LST will also be performed in the streamline-aligned coordinate, where velocity components are transformed into the localized inviscid streamline coordinates (u_s and u_c in figure 1*b*). Subscript 'str' represents quantities in streamline-aligned coordinates. Here β_{str} is calculated by projecting the total spatial wavenumber to the cross-flow direction. Note that the use of streamline-aligned coordinates is valid only within the context of local stability analysis for illustrating the symmetric and asymmetric characteristics of the first Mack mode and cross-flow mode.

Figure 4 illustrates the spatial growth rate contours at $s=40$ for the $\Lambda=0°$ case in Cartesian coordinates, the $\Lambda=45°$ case in Cartesian coordinates, the $\Lambda=45°$ case in streamline-aligned coordinates and the $\Lambda=45°$ case in streamline-aligned coordinates with u_c deliberately set to 0. Contour lines at $-\alpha_i=0.025$ are plotted to facilitate

https://doi.org/10.1017/jfm.2025.10708 Published online by Cambridge University Press

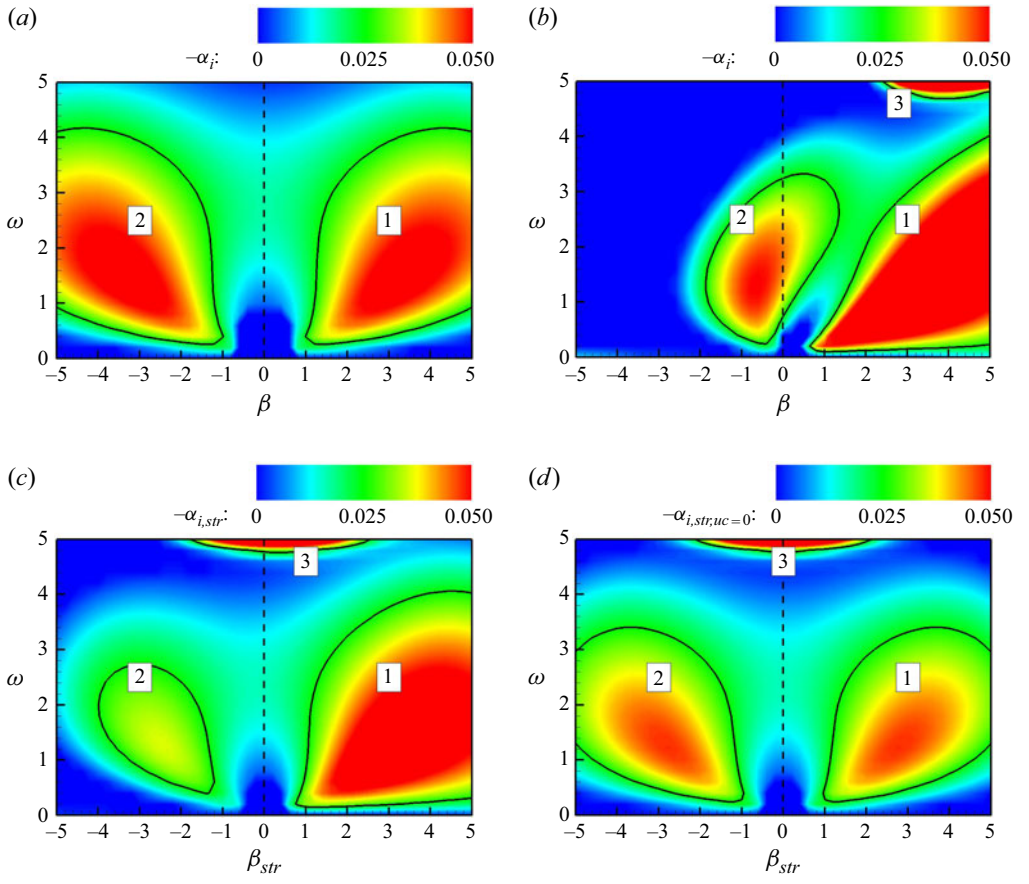


Figure 4. Growth rate contours at $s = 40$ for (*a*) the $\Lambda = 0°$ case in Cartesian coordinates and (*b*) the $\Lambda = 45°$ case in Cartesian coordinates, (*c*) the $\Lambda = 45°$ case in streamline-aligned coordinates and (*d*) the $\Lambda = 45°$ case in streamline-aligned coordinates with u_c deliberately set to 0. Black solid lines, contour lines at $-\alpha_i = 0.025$; black dashed lines, $\beta = 0$ positions.

identifying different instability regions. Positions at $\beta = 0$ are marked as dashed lines to enable observing the symmetry of instabilities.

The instability mechanism is first discussed within the Cartesian coordinate system, where velocity components u and w are employed. Since the DNS is applied in Cartesian coordinates, this LST approach enables direct comparisons in subsequent analyses. For $\Lambda = 0°$, two instability regions, which are symmetric to $\beta = 0$, span extensive ranges of β values within the lower-frequency domain. These instability regions correspond to the first Mack mode, as expected for 2-D configurations. At $\Lambda = 45°$ in Cartesian coordinates, three distinct instability regions are identified: Region 1 spans a wide range of β and connects to zero-frequency branches, typifying the emergence of cross-flow instability in the traditional terminology; Region 2, a modified mode, is confined to a narrow β region. This instability originates from the coalescence of the negative spanwise wavenumber of the first mode under the asymmetric effect of the 3-D baseflow, consistent with observations in Liu (2022) and Qiu *et al.* (2024). The asymmetry between Regions 1 and 2 also highlights the emergence of cross-flow instability. Region 3, typifying the oblique second Mack mode, occupies the high-frequency domain.

https://doi.org/10.1017/jfm.2025.10708 Published online by Cambridge University Press

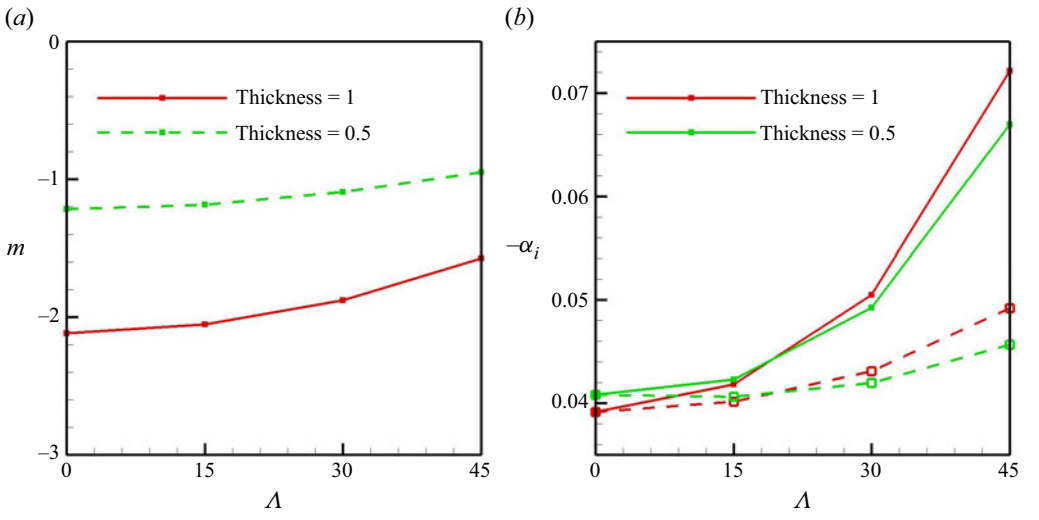


Figure 5. (*a*) Pressure gradients and (*b*) spatial growth rates at $x = 40$ in cases of different thicknesses. Solid line with filled symbols are in Cartesian coordinates; dashed line with hollow symbols are in streamline-aligned coordinates.

The LST results in the streamline-aligned coordinate are then analysed to clarify the mechanisms of each instability region. For the $\Lambda = 45°$ case in the streamline-aligned coordinate, Regions 1 and 2 remain asymmetric. Region 3 still characterizes the second Mack mode, with its maximum growth rate shifted away from $\beta = 0$. In figure 4(*d*), the cross-flow velocity is artificially set to 0, thereby illustrating the instability originating from the streamwise velocity. Compared with the $\Lambda = 0°$ case, the first mode becomes less significant and the second Mack mode shifts to lower-frequency regions. Cross-flow components universally destabilize the positive-β branch, while stabilizing the negative-β branch, confirming that cross-flow components act as a modulating mechanism rather than constituting a distinct instability mode.

As discussed before, favourable pressure gradients suppress first Mack modes (Zurigat *et al.* 1992; Masad & Zurigat 1994), while amplifying cross-flow modes (Saric & Reed 2003). A comparative analysis employs a decreased airfoil thickness of 0.5. Pressure gradients and spatial growth rates from LST at $x = 40$ for both thickness configurations and in both coordinates are summarized in figure 5. As depicted in figure 5(*a*), thinner profiles substantially decrease favourable pressure gradients across all sweep angles. Results in both coordinates reveal the same trends: at $\Lambda = 0°$ and 15°, the spatial growth rate diminishes with strengthened pressure gradients. For $\Lambda = 30°$ and 45°, the instability is amplified under an enhanced favourable pressure gradient, confirming the predominance of the cross-flow instability. Based on the instability's response to pressure gradients, the dominant mechanism is the first Mack mode when $\Lambda = 0°$ and 15°, whereas the cross-flow instability for the $\Lambda = 30°$ and 45° cases.

Although disturbances at distinct Λ exhibit differential responses to pressure gradients, both oblique first modes and cross-flow modes belong to S-modes based on LST. Figure 6 presents eigenspectra at $s = 2$, 4, 6, 8, 10, 15, 20, 25, 30, 35 and 40 for both $\Lambda = 0°$ and $\Lambda = 45°$ cases. Solid black trajectories track the evolution of the S-modes from stable to unstable states with increasing s, while green circles highlight persistently neutral F-modes. This consistent behaviour in both cases indicates a fundamental connection between these instabilities. Table 2 documents neutral point locations where the first Mack

https://doi.org/10.1017/jfm.2025.10708 Published online by Cambridge University Press

Sweep angle	0°	15°	30°	45°
Location of the neutral point	6	5.6	4.6	3.4

Table 2. Locations of neutral points for the selected mode at different sweep angles.

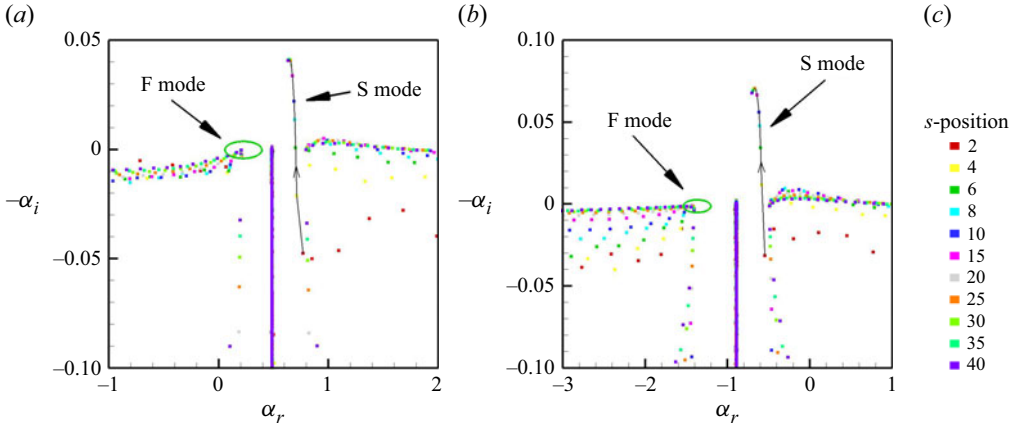


Figure 6. The evolution of F- and S-modes in (*a*) the $\Lambda = 0°$ case, (*b*) the $\Lambda = 45°$ case and (*c*) caption for both cases.

or cross-flow modes' growth rates transition to positive values. The neutral point shifts upstream with increasing sweep angles.

4. Receptivity to free stream waves

This section investigates the boundary layer receptivity mechanisms to free stream acoustic and vorticity perturbations at a circular frequency of $\omega = 0.485$ and a spanwise wavenumber of $\beta = 1.571$. As established in the prior analysis, S-modes with (without) cross-flow components serve as the dominant instability under these parametric conditions.

For unsteady calculations, small perturbations are superposed on the far-field boundary condition to simulate the receptivity process. The wave field for the receptivity simulation is expressed as

$$\boldsymbol{Q}'(x, y, z, t) = \boldsymbol{Q}(x, y, z, t) - \bar{\boldsymbol{Q}}(x, y, z) \tag{4.1}$$

where $\boldsymbol{Q}'(x, y, z, t)$ is the perturbation of a flow variable, $\boldsymbol{Q}(x, y, z, t)$ represents the instantaneous value from unsteady DNS and $\bar{\boldsymbol{Q}}(x, y, z)$ corresponds to the time-averaged values from steady DNS. The computational framework assumes spanwise-periodic conditions for swept-wing geometries, with free stream disturbance wave propagation occurring exclusively in the $x-z$ plane. For small-amplitude free stream perturbations, the perturbations of an arbitrary flow variable can be described in the following form:

$$\begin{bmatrix} u' \\ w' \\ p' \\ \rho' \end{bmatrix}_{\infty} = \begin{bmatrix} |u'| \\ |w'| \\ |p'| \\ |\rho'| \end{bmatrix}_{\infty} \exp\left(i\left[\alpha_{r,\infty}x + \beta z - \omega t\right]\right), \tag{4.2}$$

https://doi.org/10.1017/jfm.2025.10708 Published online by Cambridge University Press

where $|u'|$, $|w'|$, $|p'|$ and $|\rho'|$ represent dimensionless amplitudes of the free stream perturbations in Cartesian coordinates. The dispersion relations and perturbation magnitudes for the slow acoustic waves and vorticity waves are represented as follows (align with the definition in Ma & Zhong (2005), the usage of different axis directions causes differences on the sign):

slow acoustic waves (AC), $\omega = k_\infty(-\frac{1}{M_\infty} + \cos\theta_\infty)$,

$$\begin{aligned} |u'| &= -A\frac{M_\infty \alpha_{r,\infty}}{k_\infty}, \quad |w'| = -A\frac{M_\infty \beta}{k_\infty}, \\ |p'| &= A, \qquad\qquad |\rho'| = AM_\infty^2; \end{aligned} \tag{4.3}$$

vorticity waves (VO), $\omega = k_\infty \cos\theta_\infty$,

$$\begin{aligned} |u'| &= A\frac{\beta}{k_\infty}, \quad |w'| = -A\frac{\alpha_{r,\infty}}{k_\infty}, \\ |p'| &= 0, \qquad\qquad |\rho'| = 0. \end{aligned} \tag{4.4}$$

Hereinafter, the case nomenclature combining disturbance type and sweep angle, $AC-0°$, as an example, corresponds to the slow acoustic wave case under $\Lambda = 0°$. Here A is the dimensionless magnitude of free stream waves, set to 10^{-6} in this study. The relationships between the free stream wavenumber vector k_∞, the incident wave angle θ_∞ (see figure 1), $\alpha_{r,\infty}$ and β are

$$k_\infty = \sqrt{\alpha_{r,\infty}^2 + \beta^2} \quad \tan(\theta_\infty + \Lambda) = \beta/\alpha_{r,\infty}. \tag{4.5}$$

The current research employs perturbations with identical frequencies (ω) and spanwise wavenumbers (β) to enable systematic comparison, where ω and β are first derived from LST in § 4. The undetermined quantities, i.e. $\alpha_{r,\infty}$, k_∞ and θ_∞, are resolved by combining (4.5) with either (4.3) or (4.4). Table 3 catalogues computed $\alpha_{r,\infty}$ values across all configurations, where negative values indicate that trace velocities of the waves propagate opposite to the chordwise direction. It is important to reiterate that $\alpha_{r,\infty}$ and β are defined in the chordwise and spanwise directions. When projecting k_∞ onto the free stream velocity direction, vorticity waves always propagate with the free stream direction, not against it. After resolving these values, the free stream perturbations are introduced to the flow field by superposing the perturbations on the steady free stream variables at the far-field boundary, forming the free stream wave boundary condition. Note that linear growth phases occur upstream of $x = 40$ in all cases. Unlike the second Mack mode, neither the first Mack nor cross-flow instabilities exhibit a synchronization point between F- and S-modes, and no new flow structures emerge after linear growth onsets. Receptivity calculations are hereby restricted to the front airfoil regions ($x \leqslant 40$, the first region of the grid described in § 2) to reduce calculation cost. As the perturbations are introduced at the boundaries, 3-D unsteady DNS simulations are performed with a small time step at 1.079×10^{-4}, yielding 120 000 steps for one temporal period of the targeted perturbation. The sampling starts after $t = 150$ per 6000 steps, yielding 21 samples within a temporal period. As the study focuses on the linear receptivity process, all the dynamics are periodic, making 21 samples enough for the Fourier transformation. The time series of fluctuating pressure at $z = 0$ of the wall is processed by the Fourier transformation to obtain the phase angle ϕ'. The local wavenumber α_r of wall pressure disturbances is

https://doi.org/10.1017/jfm.2025.10708 Published online by Cambridge University Press

Sweep angle	0°	15°	30°	45°
AC	0.783	0.364	−0.039	−0.490
VO	0.485	0.081	−0.347	−0.885

Table 3. The spatial wavenumbers $\alpha_{r,\infty}$ of free stream disturbances.

subsequently calculated by (Hao & Wen 2021)

$$\alpha_r = L^* \frac{\mathrm{d}\phi'}{\mathrm{d}x}. \tag{4.6}$$

Based on the samples, the maximum wall pressure perturbation $p'_{w,max}$ is defined as the maximum absolute pressure fluctuation at the wall ($\eta = 0$) over one perturbation period and across the entire spanwise direction,

$$p'_{w,max}(x) = max_t \left(max_z \left(\left| p'(x, \eta = 0, z, t) \right| \right) \right). \tag{4.7}$$

This quantity captures the most unstable disturbance at each streamwise station, thereby representing the evolution of unstable modes.

After obtaining the perturbation field with unsteady DNS, MPT is applied on the perturbation fields for a physics-based interpretation of the receptivity process. By Helmholtz's theorem, Doak's MPT approach selects the momentum density $\boldsymbol{m}(\equiv \rho \boldsymbol{u})$ as the primary dependent vector field to be decomposed. The fluctuation momentum density $\boldsymbol{m}'$ is decomposed into the vortical component $\boldsymbol{m}'_{\boldsymbol{B}}$, acoustic component $\boldsymbol{m}'_{\boldsymbol{A}}$ and thermal component $\boldsymbol{m}'_{\boldsymbol{T}}$ as follows:

$$\boldsymbol{m}' = \boldsymbol{m}'_{\boldsymbol{B}} + \boldsymbol{m}'_{\boldsymbol{A}} + \boldsymbol{m}'_{\boldsymbol{T}}. \tag{4.8}$$

The thermal component $\boldsymbol{m}'_{\boldsymbol{T}}$ is calculated by

$$\boldsymbol{m}'_{\boldsymbol{T}} = -\nabla^2 \psi'_T = \frac{(\gamma - 1)\rho}{\gamma R} \frac{\partial S'}{\partial t}, \tag{4.9}$$

where S' is the entropy fluctuations. The acoustic component $\boldsymbol{m}'_{\boldsymbol{A}}$ is calculated by

$$\boldsymbol{m}'_{\boldsymbol{A}} = -\nabla^2 \psi'_A, \quad \psi'_A = \psi' - \psi'_T, \quad \nabla^2 \psi' = \frac{\partial \rho'}{\partial t}. \tag{4.10}$$

The vortical component $\boldsymbol{m}'_{\boldsymbol{B}}$ is subsequently calculated by (4.8). All the equations are calculated by substituting the complex perturbation vectors obtained from the Fourier transformation on the perturbation field from unsteady DNS.

These MPT components exhibit distinct physical natures. The vortical component $\boldsymbol{m}'_{\boldsymbol{B}}$ is isobaric and isentropic. The acoustic component $\boldsymbol{m}'_{\boldsymbol{A}}$ is irrotational and isentropic. The thermal component $\boldsymbol{m}'_{\boldsymbol{T}}$ is irrotational and isobaric. Such orthogonal characteristics enable MPT to systematically dissect perturbation dynamics by isolating each physical component. Comprehensive derivations of the MPT decomposition can be found in our earlier article (Lu *et al.* 2025). The momentum density components are non-dimensionalized by the free stream momentum density $\rho^*_\infty U^*_\infty$.

4.1. *Receptivity to slow acoustic waves*

The spatial evolution of perturbation fields is systematically examined through density ρ' and velocity u' distributions shown in figures 7 and 8. Figure 7 displays slices taken

https://doi.org/10.1017/jfm.2025.10708 Published online by Cambridge University Press

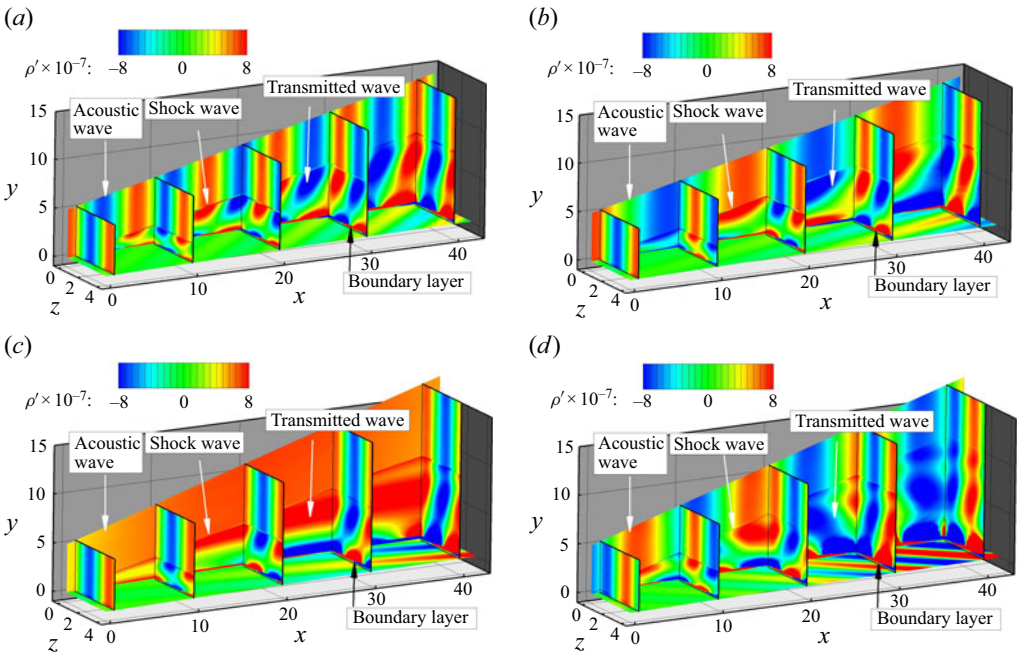


Figure 7. The density fluctuation contours of (*a*) $AC-0°$, (*b*) $AC-15°$, (*c*) $AC-30°$ and (*d*) $AC-45°$ cases.

at $z=0$, streamwise stations $x=1$, 10, 20, 30, 40 and the wall, while figure 8 details instantaneous snapshots of u' at $z=0$ and $x=30$. Shock waves and boundary layer edges are marked by white solid lines and dashed lines in figure 8. Following Balakumar's analytical framework (Balakumar 2015), the whole perturbation field comprises four distinct regions: the free stream disturbance region; the shock layer; the area between the shock and boundary layer; the boundary layer.

The first region, located outside the shock, is characterized by uniformly propagating acoustic waves, as shown in figure 7. For slow acoustic waves, the magnitude of ρ' is at the same level as that of the boundary layer disturbance, while u' is relatively small compared with the boundary layer values and consequently absent in figure 8. This originates from the magnitude relationship in (4.3). The second region encompasses the shock layer, where interactions between shock waves and slow acoustic waves result in localized amplifications of ρ'. However, u' disturbances remain too weak to be visible in figure 8. The third region between the shock and the boundary layer comprises transmitted external acoustic fields and disturbances radiating from the boundary layer. These transmitted waves soon dissipate, whereas the radiating disturbances exhibit continuous amplifications as propagating downstream. Interestingly, figure 7(*c*) reveals exclusively positive ρ' values across these three regions at $z=0$. This is attributed to the small α_r value (as shown in table 3), yielding elongated streamwise wavelengths for free stream disturbances. Free stream disturbances still propagate uniformly in this case, which can be observed in the spanwise direction from the streamwise slices, for example, $x=30$. The behaviours of acoustic waves and transmitted waves in these three regions align with 2-D receptivity simulations in Balakumar (2015) for acoustic waves, while diverging behaviours in the boundary layer arise due to distinct instability modes. Disturbances evolve and manifest as single-cell structures in the ρ' and u' fields in the boundary layers. In all scenarios, the boundary-layer disturbances start from the leading edge and rapidly surpass free

https://doi.org/10.1017/jfm.2025.10708 Published online by Cambridge University Press

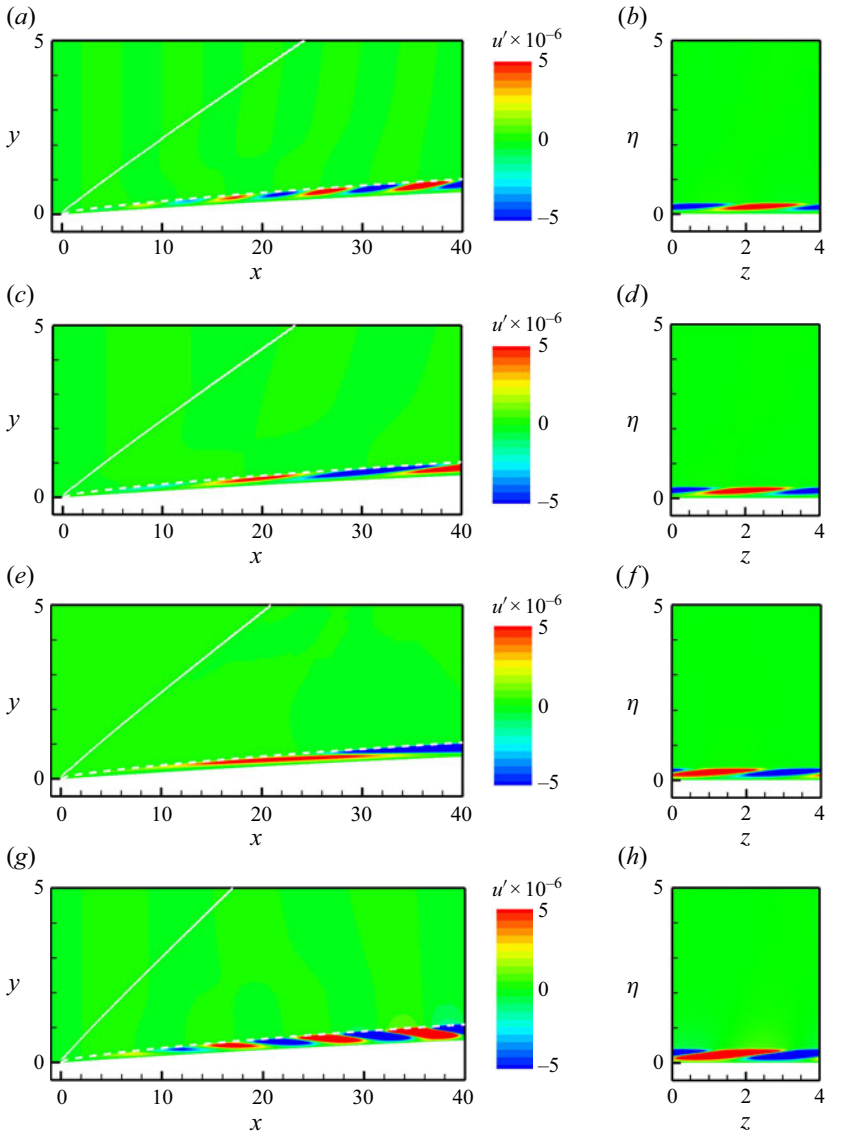


Figure 8. The streamwise velocity fluctuation contours of (*a*,*b*) $AC-0°$, (*c*,*d*) $AC-15°$, (*e*,*f*) $AC-30°$ and (*g*,*h*) $AC-45°$ cases at (*a*,*c*,*e*,*g*) $z=0$ and (*b*,*d*,*f*,*h*) $x=30$.

stream amplitudes. The disturbances within the boundary layer are critical to the transition process; therefore, they will be examined in detail through the analysis of wall pressure fluctuations.

The amplitudes and wavenumbers of wall pressure disturbances from DNS are presented in figure 9, compared with LST results. The maximum wall pressure disturbances $p'_{w,max}$ from the DNS are plotted, along with N factors from LST for comparison. The N factors follow the definition in van Ingen (2008):

$$N=\int_{x_{neutral}}^{x}-\alpha_i \mathrm{d}x=\ln(A_x/A_0). \tag{4.11}$$

https://doi.org/10.1017/jfm.2025.10708 Published online by Cambridge University Press

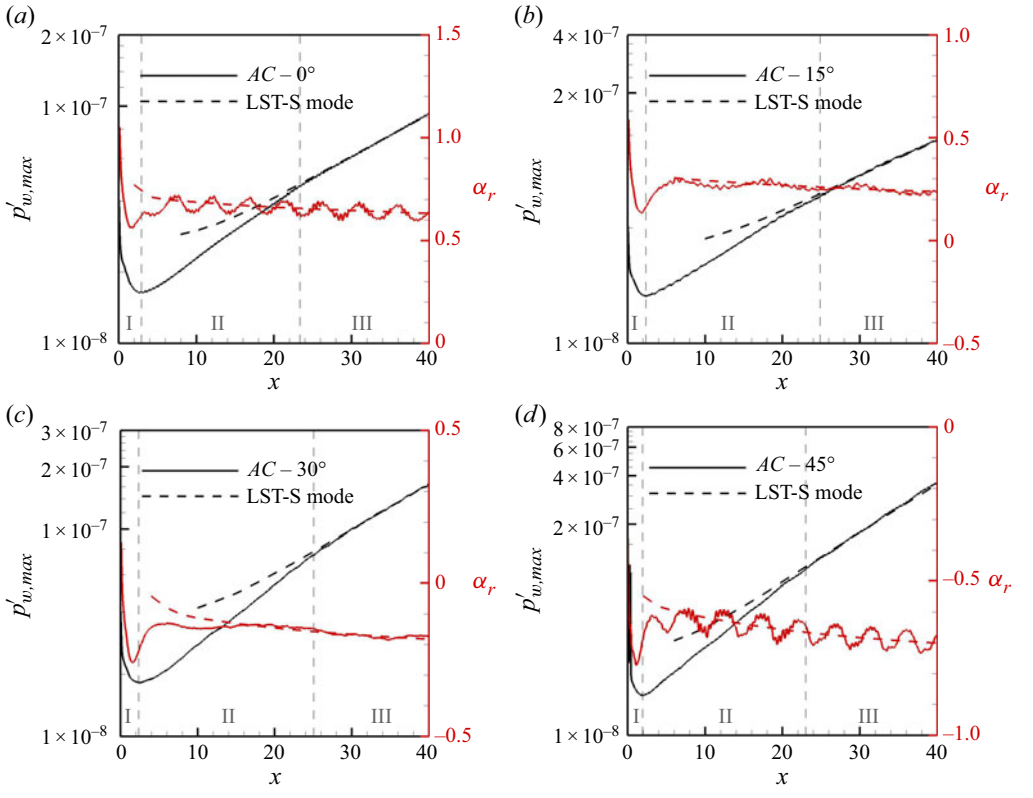


Figure 9. The wall pressure fluctuation amplitudes and streamwise wavenumbers for (*a*) $AC-0°$, (*b*) $AC-15°$, (*c*) $AC-30°$ and (*d*) $AC-45°$ cases.

The N factor is calculated by integrating the growth rate from the neutral point $x_{neutral}$ to streamwise location x in LST. This equals the natural logarithm of the ratio of the disturbance amplitude A_x to an initial amplitude A_0. This relationship enables direct comparison between $p'_{w,max}$ and N factors: for case $AC-0°$, the $p'_{w,max}$ axis spans 1×10^{-8} to 2×10^{-7}, corresponds to an N-factor range $\ln(2\times10^{-7}/1\times10^{-8})\approx2.996$. The N factor is plotted on a linear scale preserving this range, with $x>23$ aligned with $p'_{w,max}$, confirming the onset of linear growth. This approach enables visual comparison between DNS and LST results. The N factor axis is then hidden for figure conciseness. The formation of the targeted S-modes goes through: Stage I, a leading-edge damping stage; Stage II, an enhanced exponential growth stage; and finally Stage III, the linear growth stage. The leading-edge damping and enhanced exponential growth stage are separated by the minimum value of $p'_{w,max}$. Farther downstream, the emergence of a linear growth stage is defined as the location where the DNS and LST results are highly aligned. For oscillating α_r from DNS, it should be closely around LST values. Dark grey lines in figure 9 mark the onsets of enhanced exponential growth and linear growth.

The results indicate first Mack and cross-flow modes undergo a uniform receptivity pathway. At the leading edges, the interactions between acoustic waves, shock waves and boundary layers induce sudden amplitude enlargement followed by rapid damping, accompanied by abrupt α_r shift. After the local minimum of $p'_{w,max}$, perturbation growth rates surpass LST predictions, represented by the larger slopes from DNS, along with the wavenumbers gradually converge towards S-mode values, forming an enhanced

https://doi.org/10.1017/jfm.2025.10708 Published online by Cambridge University Press

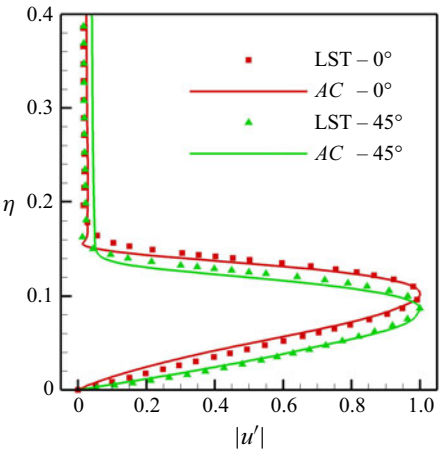


Figure 10. The u' profiles for $AC-0°$ and $AC-45°$ cases at neutral points.

exponential growth stage. During this region, wavenumbers approach S-mode values sooner than the amplitudes, implying the perturbations possess some key features of the S-mode before the onset of linear growth. This is corroborated by u'-profiles at the neutral point (as depicted in figure 10), where cases $AC-0°$ and $AC-45°$ exhibit strong agreement with LST eigenfunctions prior to linear growth phases. After enhanced exponential growth, both spatial growth rates and wavenumbers of perturbations align with LST solutions, indicating linear growths of the targeted S-modes occur. Two fundamental questions arise from these observations: Why does rapid damping occur at the leading edge despite the synchronization between S-modes and slow acoustic waves? How does the enhanced exponential growth happens when perturbation profiles already approximate S-mode eigenfunctions? The underlying mechanisms of this receptivity pathway are then discussed with MPT.

Instantaneous snapshots of MPT component, defined as $\boldsymbol{m'_{A,BorT}} = Re(m'_{A,BorT,x}) + Re(m'_{A,BorT,y}) + Re(m'_{A,BorT,z})$, in $AC-0°$ and $AC-45°$ cases are illustrated in figure 11. Shock waves and boundary layer edges are marked by white solid lines and dashed lines, whereas the vertical black dashed line indicates the beginning of enhanced exponential growth and linear growth stages. Momentum potential theory components exhibit distinct behaviours in different regions: in the free stream disturbance region, the acoustic component $\boldsymbol{m'_A}$ propagates uniformly, whereas $\boldsymbol{m'_B}$ and $\boldsymbol{m'_T}$ remain negligible in the free stream. At the shock layer, $\boldsymbol{m'_A}$ experiences localized distortion, accompanied by weak $\boldsymbol{m'_B}$ generation due to baroclinity, while $\boldsymbol{m'_T}$ persists at negligible levels. The postshock transmitted waves are composed of acoustic and vortical waves.

Figure 12 depicts the amplitudes of MPT components at $s=1$, 20, 40, aiming to capture the leading-edge damping, enhanced exponential growth and linear growth behaviours. Each amplitude is normalized by the maximum fluctuation momentum density $\boldsymbol{m'}$ in boundary layers. During the linear growth stage (the $s=40$ profile), $\boldsymbol{m'_B}$ is the dominant component, exceeding both $\boldsymbol{m'_A}$ and $\boldsymbol{m'_T}$ in magnitudes by orders, which reflects the vortical nature of the targeted modes. This vortical-dominant behaviour aligns with our prior findings for cross-flow instabilities (Lu *et al.* 2025).

For the disturbance evolution in boundary layer regions, the receptivity stages is explained by MPT component dynamics. At the leading-edge, significant $\boldsymbol{m'_A}$ is generated through the synchronization mechanism (Xu *et al.* 2018). Here $\boldsymbol{m'}$ rapidly decays as this

https://doi.org/10.1017/jfm.2025.10708 Published online by Cambridge University Press

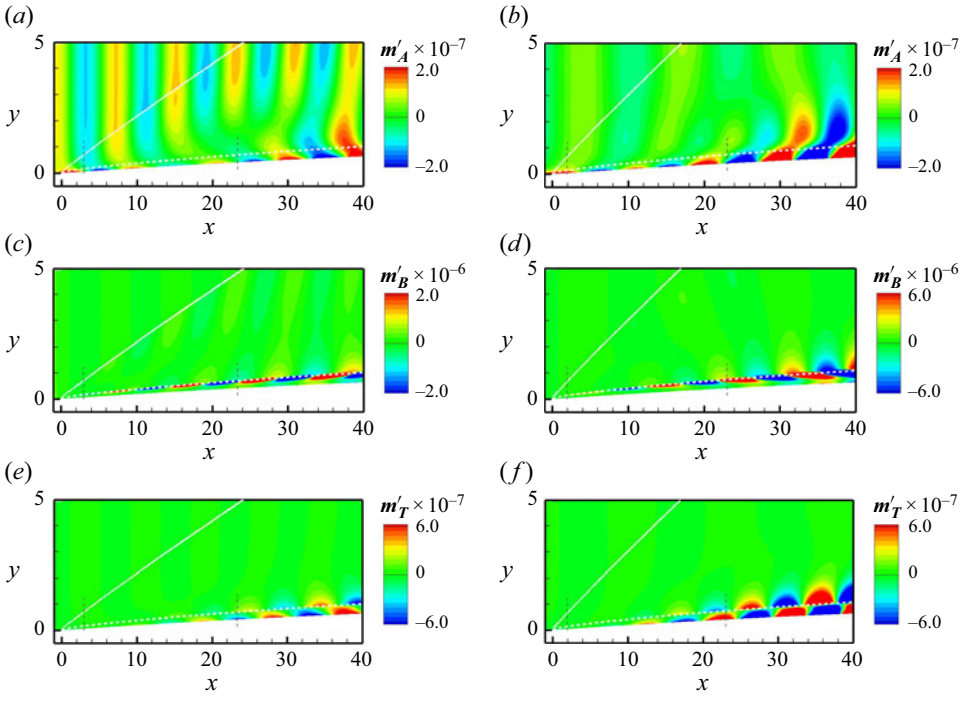


Figure 11. The instantaneous snapshots of (*a*,*b*) acoustic components, (*c*,*d*) vortical components, (*e*,*f*) and thermal components in (*a*,*c*,*e*) $AC-0°$ and (*b*,*d*,*f*) $AC-45°$ cases.

large acoustic component cannot persist in boundary layers. Concurrently, $\boldsymbol{m'_B}$ makes up a smaller proportion than the linear stage, while $\boldsymbol{m'_T}$ constitutes a large fraction. The high amplitude and fast dissipation at the leading edge observed in figure 9 correspond to the damping of acoustic perturbations. During the enhanced exponential growth stage, $\boldsymbol{m'_A}$ dissipates to a small proportion, with $\boldsymbol{m'_T}$ reducing to a lower level than the linear growth. In figures 11(*c*,*d*) and 12(*b*,*e*), $\boldsymbol{m'_B}$ exhibits continuous growth in magnitudes from $s=1$ to 20. The predominance of $\boldsymbol{m'_B}$ near the neutral point results in the good agreement between perturbation profiles and LST eigenfunctions in figure 10, since the vortical component is the primary contributor to the targeted S-modes. In this stage, the adjustment of $\boldsymbol{m'_A}$ and $\boldsymbol{m'_T}$ drive $p'_{w,max}$ and α_r towards convergence with LST results, whereas the high growth rate is credited to the growth of $\boldsymbol{m'_B}$. Farther downstream, all MPT components enter a steady growth phase, signalling the free stream acoustic waves successfully excite the targeted S-modes, thereby completing the receptivity process.

Both $AC-0°$ and $AC-45°$ cases share the same receptivity mechanisms, with their divergence manifesting in amplitudes of MPT components. The underlying mechanisms of the receptivity pathway can be summarized as: $\boldsymbol{m'_A}$ initially penetrates the boundary layer at high proportions, subsequently undergoing damping and recovery; $\boldsymbol{m'_B}$ exhibits continuous growth throughout the receptivity process; $\boldsymbol{m'_T}$ goes through a similar pathway with $\boldsymbol{m'_A}$ but with lower initial proportions among the three components.

The receptivity coefficient refers to the efficiency of disturbance waves in generating instability waves, thus is a crucial factor in engineering. According to Balakumar's definition (Balakumar & King 2011), the receptivity coefficient to slow acoustic waves is defined at the neutral point, formed as

https://doi.org/10.1017/jfm.2025.10708 Published online by Cambridge University Press

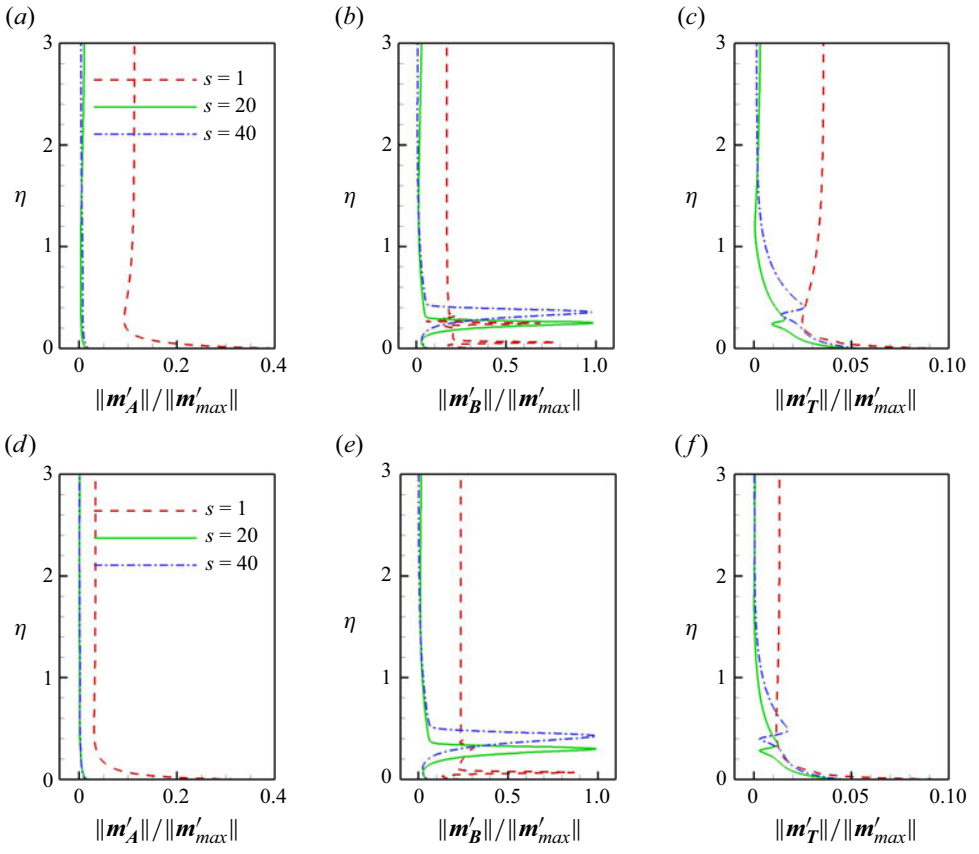


Figure 12. The normalized amplitudes of (*a*,*d*) acoustic components, (*b*,*e*) vortical components, and (*c*,*f*) thermal components in $AC-0°$ (*a*,*b*,*c*) and $AC-45°$ (*d*,*e*,*f*) cases.

$$C_{AC} = \left(u'_{max}/|p'|_{AC}\right)_{neutral}. \tag{4.12}$$

As neutral points lie in enhanced exponential growth stages, where dynamics are governed by the behaviour of increasing $\boldsymbol{m}'_{\boldsymbol{B}}$, this metric effectively quantifies the efficiency of acoustic waves in exciting vortical components, offering practical insight for engineering applications. The receptivity coefficients to slow acoustic waves for various sweep angles are summarized by the red line in figure 13. Here C_{AC} demonstrates a consistent decrease as the sweep angle increases. The absence of abrupt discontinuities in C_{AC} when the sweep angle increases further highlights that these two instabilities are of the same nature.

4.2. *Receptivity to vorticity waves*

Consistent with (4.4), vorticity waves are introduced into the flow field. Figure 14 illustrates the spatial distributions of u' across all cases with vorticity disturbances. White solid lines are plotted in the $z=0$ slice to mark the shock wave positions. Instantaneous snapshots of ρ' at $z=0$ and $x=30$ are presented in figure 15. Shock waves and boundary layer edges are marked by white solid lines and dashed lines. Given the unique receptivity behaviour associated with vorticity waves, perturbation fields near leading edges are presented in zoomed-in views to facilitate observation. The flow field is also divided into four regions: the free stream disturbance region; the shock layer; the area between the shock and boundary layer; the boundary layer.

https://doi.org/10.1017/jfm.2025.10708 Published online by Cambridge University Press

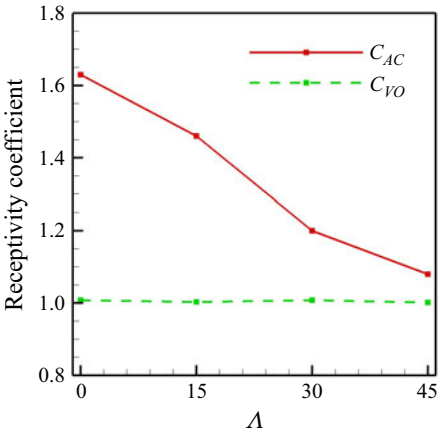


Figure 13. The receptivity coefficients of all cases.

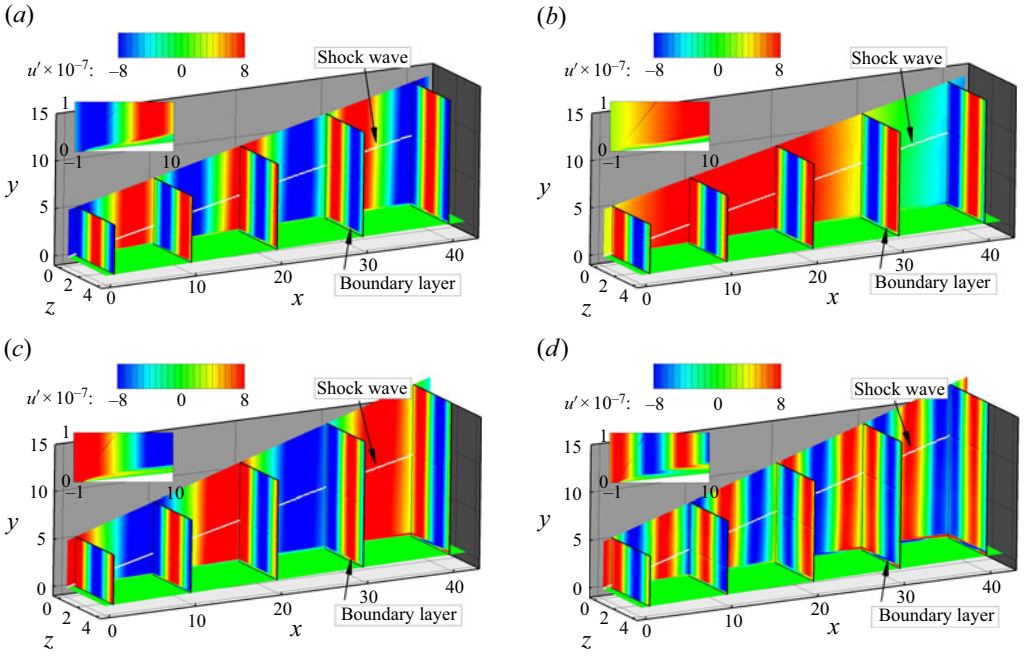


Figure 14. The streamwise velocity fluctuation contours of (*a*) $VO-0°$, (*b*) $VO-15°$, (*c*) $VO-30°$ and (*d*) $VO-45°$ cases.

In the free stream disturbance regions, only velocity disturbances (u') are observed, while ρ' remain absent, consistent with the governing relation defined in (4.4). Shock layers generate density disturbances at a comparable order of magnitude to those in the boundary layer, while changes in u' are small. Impacts of weak leading-edge shock waves on vorticity disturbances are less significant than that on slow acoustic waves. The transmitted waves closely resemble vorticity waves and connect to boundary layers,

https://doi.org/10.1017/jfm.2025.10708 Published online by Cambridge University Press

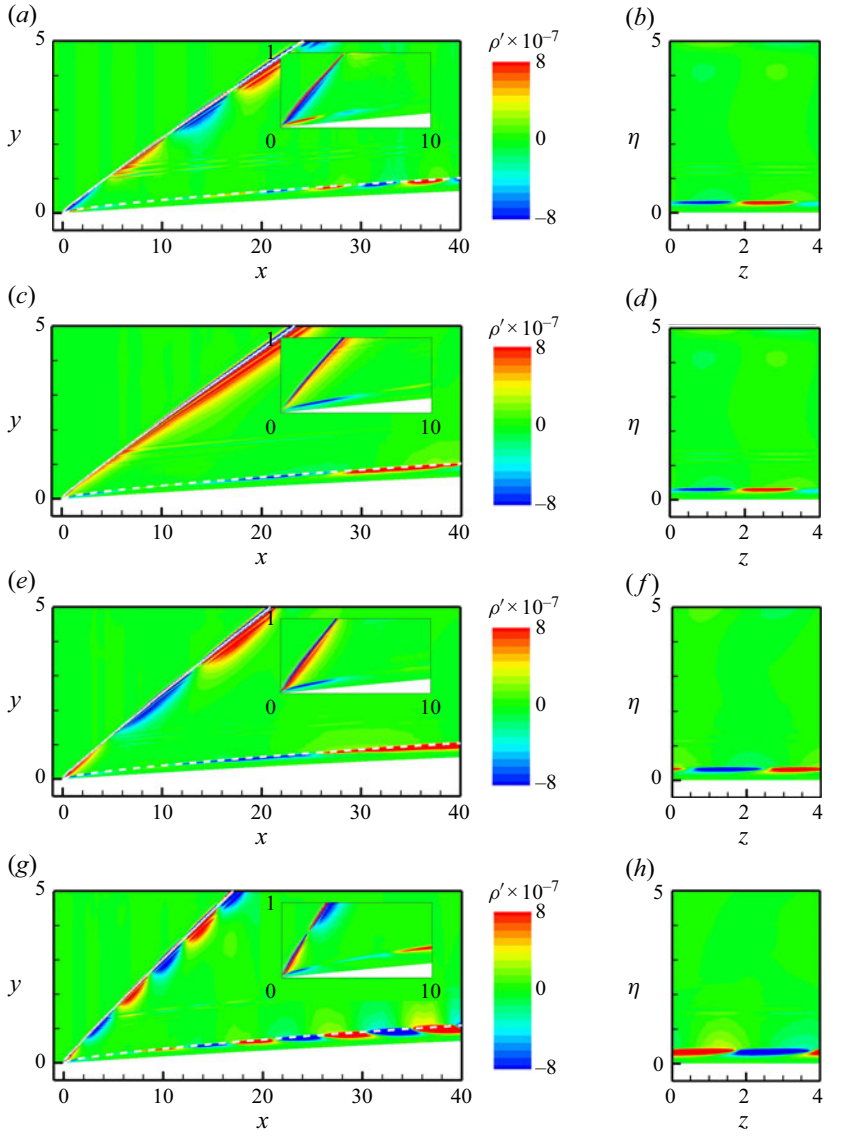


Figure 15. The density fluctuation contours of (*a*,*b*) $VO-0°$, (*c*,*d*) $VO-15°$, (*e*,*f*) $VO-30°$ and (*g*,*h*) $VO-45°$ cases at (*a*,*c*,*e*,*g*) $z=0$ and (*b*,*d*,*f*,*h*) $x=30$.

which complicate the identification of unstable modes with u' in boundary layers. A practical method for identifying unstable modes is to observe ρ' in figure 15. Disturbances with short spatial wavelengths are generated through the interaction between shock waves, vorticity waves and boundary layers at the leading edge. These disturbances dissipate quickly, forming 'dead zones', which are characterized as the relatively low magnitudes of perturbations. Downstream of these 'dead zones', the targeted S-modes are established. Within a considerable distance (until approximately $x=30$), u' amplitudes within boundary layers remain smaller than the free stream perturbation levels (see figure 14).

https://doi.org/10.1017/jfm.2025.10708 Published online by Cambridge University Press

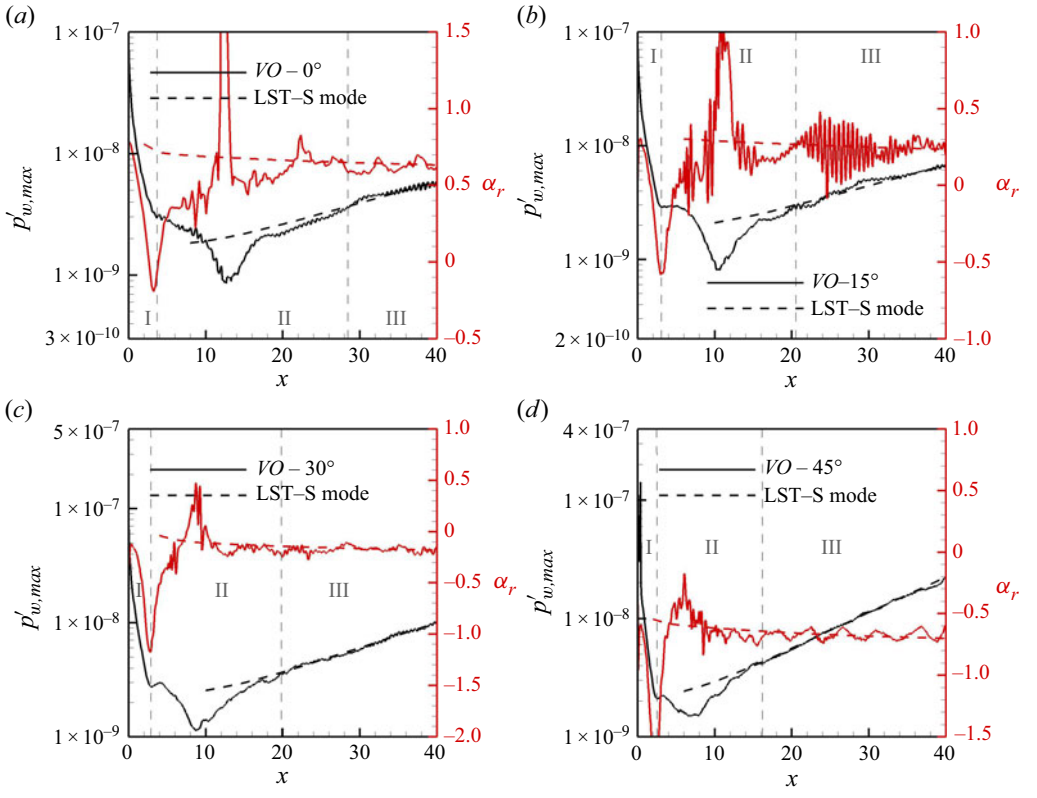


Figure 16. The wall pressure fluctuation amplitudes and streamwise wavenumbers for (*a*) $VO-0°$, (*b*) $VO-15°$, (*c*) $VO-30°$ and (*d*) $VO-45°$ cases.

Figure 16 summarizes the amplitudes and spatial wavenumbers of wall pressure disturbances from DNS, along with N factors and α_r of S-modes from LST. In all cases, three stages are identified: Stage I the leading-edge damping, identified by the steep reduction in both perturbation amplitudes and α_r; Stage II a non-modal stage, characterized by a secondary decrease of $p'_{w,max}$ and recovery; Stage III the linear growth stage. The beginnings of non-modal and linear growth are marked by vertical black lines. Prior studies suggest that F-modes are easily excited by vorticity waves (Ma & Zhong 2005; Balakumar 2015). However, the leading-edge wavenumbers are incompatible with F-modes, indicating this mechanism does not occur under current flow configurations, where F-modes remain neutral throughout the boundary layer (depicted in figure 6). The decline of $p'_{w,max}$ and α_r at the leading-edge peak ($x < 4$) is similar to the leading-edge decline observed in acoustic wave cases (figure 9, $x = 0$–4). This parallel demonstrates that the dissipation may act as the governing mechanism in this stage. Following this dissipating stage, $p'_{w,max}$ exhibit secondary decrease and recovery (very weak in the $VO-45°$ case), corresponding to the 'dead zone' observed in figure 15. During this regime, α_r surpass LST predictions. Finally, linear growth occurs in Stage III, where both $p'_{w,max}$ growth and α_r converge with LST predictions. Interestingly, non-modal stages induced by acoustic waves remain nearly constant across different sweep angles, while the

https://doi.org/10.1017/jfm.2025.10708 Published online by Cambridge University Press

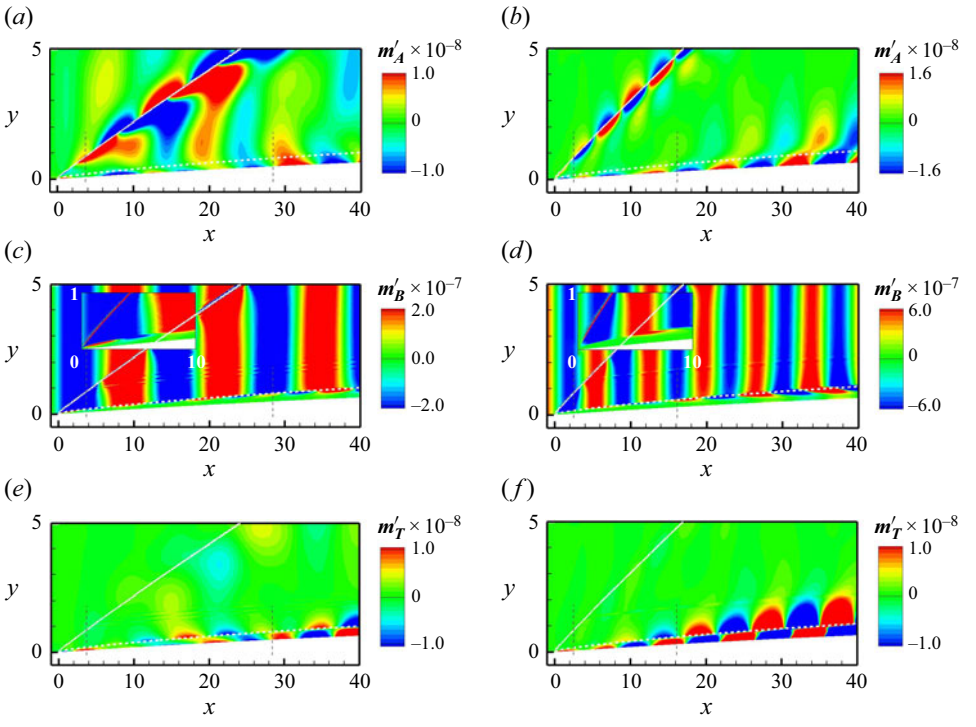


Figure 17. The instantaneous snapshots of (*a*,*b*) acoustic components, (*c*,*d*) vortical components and (*e*,*f*) thermal components for (*a*,*c*,*e*) $VO-0°$ and (*b*,*d*,*f*) $VO-45°$ cases.

non-modal stages persist for a shorter extent under larger sweep angles, implying a stronger receptivity to vorticity waves caused by cross-flow components.

Instantaneous snapshots of MPT components for the $VO-0°$ and $VO-45°$ cases are presented in figure 17. Shock waves and boundary layer edges are marked by white solid lines and dashed lines, whereas the vertical black dashed lines refer to the beginning of non-modal growth and linear growth stages. As both the incoming perturbations and S-modes are of a vortical nature, the receptivity process in *VO* cases mainly involves the behaviours of $\boldsymbol{m}'_{\boldsymbol{B}}$. Magnified views of $\boldsymbol{m}'_{\boldsymbol{B}}$ near the leading edge are included to highlight its behaviour. Upstream of shock waves, $\boldsymbol{m}'_{\boldsymbol{B}}$ is uniformly transported by the free stream vorticity waves, while $\boldsymbol{m}'_{\boldsymbol{A}}$ are observed due to the contamination from the shock layer. At the shock layer, $\boldsymbol{m}'_{\boldsymbol{A}}$ undergoes significant generation, alongside weaker $\boldsymbol{m}'_{\boldsymbol{T}}$ generation, while $\boldsymbol{m}'_{\boldsymbol{B}}$ is locally disturbed. Notably, within the shock layer, $\boldsymbol{m}'_{\boldsymbol{A}}$ achieves higher amplitudes compared with its presence in the boundary layer, whereas $\boldsymbol{m}'_{\boldsymbol{T}}$ is less prominent. The transmitted waves remain predominantly vortical in composition. At the boundary layer edge, figures 17(*c*) and 17(*d*) reveal a distinctive phenomenon: the vorticity components are effectively blocked from the boundary layer. This observation aligns with the inference of Fedorov & Khokhlov (2001) that the boundary layer effectively swallows vorticity waves. These results provide direct support that the primary source of boundary-layer modes originates from the interactions at the leading edge, with external vorticity waves contributing as a secondary mechanism, transferring limited energy at the boundary-layer edge.

https://doi.org/10.1017/jfm.2025.10708 Published online by Cambridge University Press

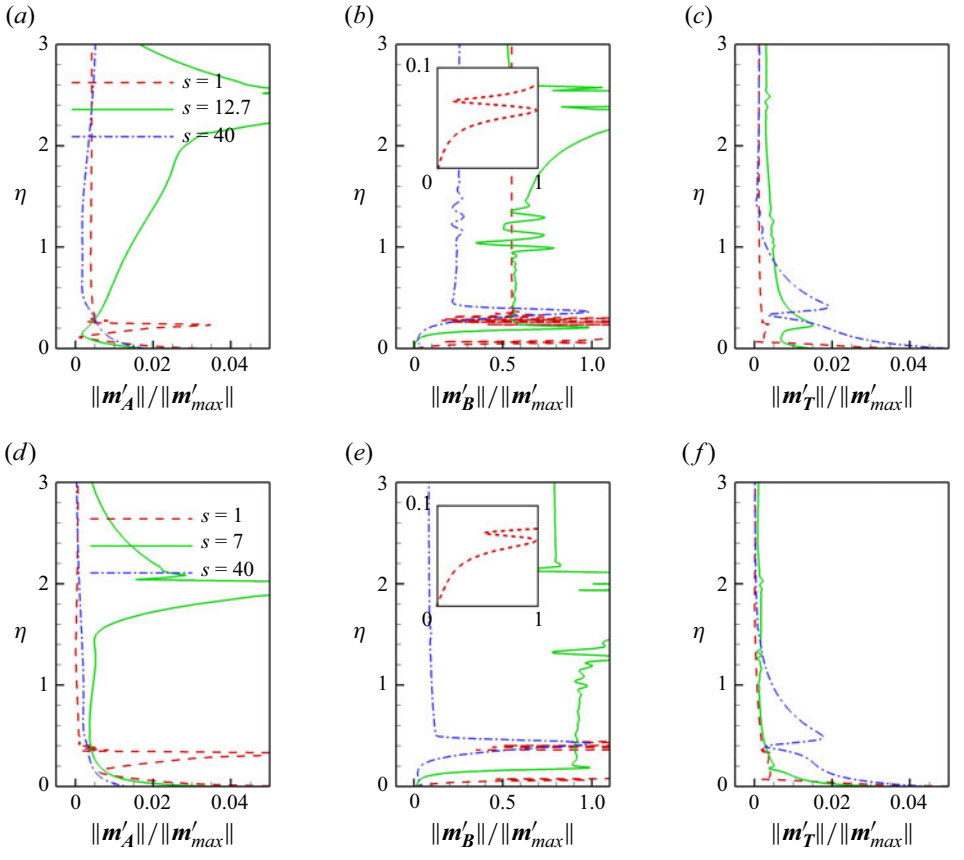


Figure 18. The normalized amplitudes of (*a*,*d*) acoustic components, (*b*,*e*) vortical components and (*c*,*f*) thermal components in (*a*,*c*,*e*) *VO* − 0° and (*b*,*d*,*f*) *VO* − 45° cases.

Figure 18 depicts the amplitudes of MPT components at $s = 1$, 7 or 12.7, 40, aiming to capture the leading edge, non-modal stage and linear growth behaviours. The second slices are selected at the minimum of $p'_{w,max}$ to capture the 'dead zone' behaviour. Each amplitude is normalized by the maximum fluctuation momentum density $\boldsymbol{m}'$ in the boundary layers. The transmitted wave at $s = 1$ is stronger than the boundary layer disturbances. The peak of this slice is plotted in a zoomed-in view for $\boldsymbol{m}'_{\boldsymbol{B}}$. Unlike *AC* cases, the interactions between the vorticity wave, shock wave and boundary layer produce strong acoustic and vortical components, whereas thermal components exhibit lower proportions compared with the linear growth stage. This indicates the leading-edge damping of *VO* cases is not induced solely by the acoustic component. In the subsequent non-modal stage, $\boldsymbol{m}'_{\boldsymbol{A}}$ and $\boldsymbol{m}'_{\boldsymbol{T}}$ both exhibit lower proportions compared with the leading-edge profile, forming the secondary decrease of $p'_{w,max}$ in figure 16. Changes in $\boldsymbol{m}'_{\boldsymbol{A}}$, $\boldsymbol{m}'_{\boldsymbol{T}}$ and the secondary decrease in case $V0 - 45°$ are less pronounced. From figures 17(*c*) and 17(*d*), $\boldsymbol{m}'_{\boldsymbol{B}}$ seems to undergo modulation at the wavelengths during this stage, whereas $\boldsymbol{m}'_{\boldsymbol{A}}$ and $\boldsymbol{m}'_{\boldsymbol{T}}$ undergo attenuation and recovery. Subsequently, the linear growth phase

https://doi.org/10.1017/jfm.2025.10708 Published online by Cambridge University Press

commences, enabling boundary-layer modes to develop in a manner consistent with LST. The proportions of MPT components become highly similar to *AC* cases in figure 12.

The $VO-0°$ and $VO-45°$ cases also share the same receptivity mechanisms, with their divergence manifesting in amplitudes of MPT components. The underlying mechanisms of the receptivity pathway can be summarized as: $\boldsymbol{m}'_{\boldsymbol{B}}$ initially penetrates the boundary layer as a dominant component, then undergo adjustments to fit the linear growth. Here $\boldsymbol{m}'_{\boldsymbol{A}}$ and $\boldsymbol{m}'_{\boldsymbol{T}}$ attenuates initially but recovers downstream. These parallels highlight the same physical nature of the first Mack and cross-flow modes.

The receptivity coefficients are then calculated with the definition in Balakumar & King (2011):

$$C_{VO} = \left(u'_{max}/|u'|_{VO}\right)_{neutral}. \tag{4.13}$$

These coefficients are summarized in figure 13. All the receptivity coefficients are nearly unity because the neutral points align with the dissipating phase of leading-edge disturbances. This situation renders them inadequate for effectively quantifying the genuine efficiency of vorticity waves in inducing unstable modes.

5. Conclusions

The receptivity of a spanwise-infinite wing to 3-D slow acoustic waves and vorticity waves at various sweep angles has been comprehensively investigated. The LST was utilized to provide a preliminary prediction of the properties of the relevant instabilities, offering a foundational understanding. Then DNS was employed to obtain the detailed perturbation fields, capturing the precise dynamics of the receptivity processes. Furthermore, the MPT decomposition was employed to analyse these receptivity processes in detail, providing insight into the generation and evolution of boundary-layer instabilities.

For the baseflows, the sharp wing configuration with a constant curvature establishes a nearly constant favourable pressure gradient downstream of the leading edge. As the sweep angle increases, there is a noticeable rise in both the cross-flow velocity and the boundary layer thickness. The LST categorizes both the first Mack modes and cross-flow instabilities as S-modes. At the prescribed frequency and spanwise wavelength, S-modes convert to an unstable state in the downstream region, whereas F-modes remain neutral across the boundary layer. With increasing sweep angle, the location of the neutral point for the dominant modes shifts upstream. The dominant instability is the first mode at $\Lambda = 0°$ and $15°$, whereas the cross-flow mode becomes dominant when $\Lambda = 30°$ and $45°$.

First and cross-flow modes go through the same receptivity pathway to slow acoustic waves: a strong perturbation with large α_r is generated through the synchronization mechanism at the leading edge. Strong acoustic components ($\boldsymbol{m}'_{\boldsymbol{A}}$) are produced through synchronization. Then a rapid damping of disturbance amplitudes and α_r happens as this strong acoustic component cannot persist in boundary layers. Then the non-modal growth exhibits a higher growth rate than that of the S-mode, and α_r deviates slightly from the S-mode. In this phase, high growth rates are governed by the continuous growth of the vortical components ($\boldsymbol{m}'_{\boldsymbol{B}}$), meanwhile adjustments of $\boldsymbol{m}'_{\boldsymbol{A}}$ and the thermal component ($\boldsymbol{m}'_{\boldsymbol{T}}$) drive the convergence of $p'_{w,max}$ and α_r to LST predictions. The linear growth stage begins after the MPT components adjust and the results of DNS and LST match each other. At this final stage, $\boldsymbol{m}'_{\boldsymbol{B}}$ is the dominant component, exceeding both $\boldsymbol{m}'_{\boldsymbol{A}}$ and $\boldsymbol{m}'_{\boldsymbol{T}}$ in magnitude. The oblique first mode and travelling cross-flow mode are both of a vortical

https://doi.org/10.1017/jfm.2025.10708 Published online by Cambridge University Press

nature. The receptivity coefficient demonstrates a consistent decrease as the sweep angle increases.

The receptivity to vorticity waves of these two modes is also consistent, while the pathway is different from acoustic wave cases: at the leading edge, disturbances are generated at the leading edge through the complex interactions between the incoming vorticity wave, the shock wave and the boundary layer. These disturbances comprise mainly $\boldsymbol{m}'_{\boldsymbol{B}}$ and undergo leading-edge dissipation. Then disturbances enter a non-modal stage. In this phase, $\boldsymbol{m}'_{\boldsymbol{B}}$ undergo spatial reshaping, whereas $\boldsymbol{m}'_{\boldsymbol{A}}$ and $\boldsymbol{m}'_{\boldsymbol{T}}$ undergo attenuation and recovery. Finally, the MPT components achieve equilibrium, and the linear growth occurs. In vorticity wave cases, all the receptivity coefficients are nearly unity. The receptivity coefficient is ineffective for quantifying the capability on exciting unstable modes.

The current results highlight the consistency between oblique first Mack modes and travelling cross-flow modes in hypersonic boundary layers: both instabilities are of inviscid type by an inflection point or generalized inflection point, and belong to S-modes. The vortical component $\boldsymbol{m}'_{\boldsymbol{B}}$ is the dominant component in both instabilities for their linear growth. The receptivity processes of both instabilities to slow acoustic waves and vorticity waves do not show qualitative differences. These observations suggest that the first and cross-flow modes are of the same nature.

Based on the unified characterization of first and cross-flow instabilities as inherently consistent S-modes, systematic parametric studies are required to quantify the impacts of flow parameters, i.e. Mach number and Reynolds number, on these instabilities. This unified understanding sheds light on the design of laminar control techniques. Control methods such as wall cooling and blowing–suction may be refined within a unified framework, potentially reducing the cost of such techniques.

Acknowledgements. We would like to express our honest appreciation to Professor X. Li for his generosity in providing the DNS codes, and Professor L. Zhao for his useful dicussions and suggestions.

Funding. This study was supported by the National Natural Science Foundation of China (NSFC grants no. 12272049) and the Research Grants Council, Hong Kong, under contract nos. 15216621 and 15203724.

Declaration of interests. The authors report no conflict of interest.

Data availability statement. The data that support the findings of this study are available from the corresponding author upon reasonable request.

Appendix. Grid independence validation

This appendix validates grid independence through comparisons of baseflow and unsteady quantities. The baseline coarse grid (detailed in § 2) was refined by factors of 1.5 in the streamwise (x) and wall-normal (y) directions and 2 in spanwise (z) direction within the leading-edge region (red region marked in figure 1d), yielding $1321 \times 751 \times 41$ grid dimensions. The background and sponge regions comprise $381 \times 751 \times 41$ and $21 \times 751 \times 41$ grid points, respectively, resulting in a total dense grid dimension of $1721 \times 751 \times 41$. Figures 19($a$) and 19($b$) present u and T profiles at $x = 10, 20, 30, 40$ for case $VO - 45°$ computed on both grids. Figures 19(c) and 19(d) show instantaneous wall pressure fluctuations for case $VO - 45°$ at $t = 77.0486$ across both resolutions, with unsteady flow validation restricted to $x < 20$ to reduce computational cost. The high agreement between the two grids confirms the grid independence.

https://doi.org/10.1017/jfm.2025.10708 Published online by Cambridge University Press

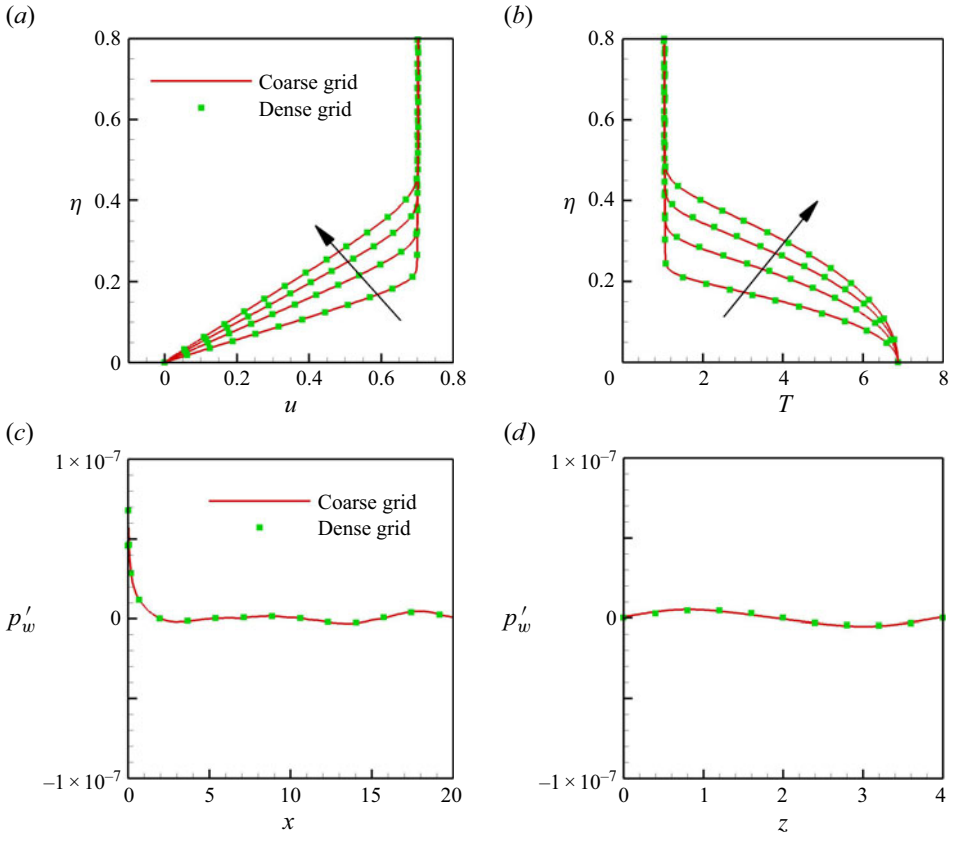


Figure 19. The (*a*) u profiles, (*b*) T profiles, (*c*) instantaneous wall pressure fluctuations at $z = 0$ and (*d*) instantaneous wall pressure fluctuations at $x = 20$ for case $VO - 45°$ with different grid dimensions.

References

Balakumar, P. 2015 Receptivity of hypersonic boundary layers to acoustic and vortical disturbances (invited), In *45th AIAA Fluid Dynamics Conference*, American Institute of Aeronautics and Astronautics.

Balakumar, P. & Kegerise, M.A. 2015 Receptivity of hypersonic boundary layers over straight and flared cones. *AIAA J.* **53** (8), 2097–2109.

Balakumar, P. & King, R. 2011 Receptivity to roughness, acoustics, and vortical disturbances in supersonic boundary layers over swept wings, In *41st AIAA Fluid Dynamics Conference and Exhibit*, American Institute of Aeronautics and Astronautics.

Balakumar, P. & King, R.A. 2012 Receptivity and stability of supersonic swept flows. *AIAA J.* **50** (7), 1476–1489.

Chen, J., Dong, S., Chen, X., Yuan, X. & Xu, G. 2021*a* Stationary cross-flow breakdown in a high-speed swept-wing boundary layer. *Phys. Fluids* **33** (2), 024108.

Chen, J., Yi, S., Li, X., Han, G., Zhang, Y., Yang, Q. & Yuan, X.2021*b* Theoretical, numerical and experimental study of hypersonic boundary llayer transition: blunt circular cone. *Appl. Therm. Engng.* **194**, 116931.

Chen, Y., Tu, G., Wan, B., Su, C., Yuan, X. & Chen, J. 2021*c* Receptivity of a hypersonic flow over a blunt wedge to a slow acoustic wave. *Phys. Fluids* **33** (8), 084114.

Chen, X., Dong, S., Tu, G., Yuan, X. & Chen, J.2022 Boundary layer transition and linear modal instabilities of hypersonic flow over a lifting body. *J. Fluid Mech.* **938**, A8.

Chen, X., Zhu, Y. & Lee, C. 2017 Interactions between second mode and low-frequency waves in a hypersonic boundary layer. *J. Fluid Mech.* **820**, 693–735.

Craig, S.A. & Saric, W.S. 2016 Crossflow instability in a hypersonic boundary layer. *J. Fluid Mech.* **808**, 224–244.

https://doi.org/10.1017/jfm.2025.10708 Published online by Cambridge University Press

DEYHLE, H. & BIPPES, H. 1996 Disturbance growth in an unstable three-dimensional boundary layer and its dependence on environmental conditions. *J. Fluid Mech.* **316**, 73–113.
DOAK, P.E. 1989 Momentum potential theory of energy flux carried by momentum fluctuations. *J. Sound Vib.* **131** (1), 67–90.
DOAK, P.E. 1998 Fluctuating total enthalpy as the basic generalized acoustic field. *Theor. Comput. Fluid Dyn.* **10** (1–4), 115–133.
FEDOROV, A. 2002 Receptivity of high speed boundary layer to acoustic disturbances (invited), In *32nd AIAA Fluid Dynamics Conference and Exhibit*, American Institute of Aeronautics and Astronautics.
FEDOROV, A. 2011 Transition and stability of high-speed boundary layers. *Annu. Rev. Fluid Mech.* **43** (2011), 79–95.
FEDOROV, A. & KHOKHLOV, A. 2001 Prehistory of instability in a hypersonic boundary layer. *Theor. Comput. Fluid Dyn.* **14**, 359–375.
FEDOROV, A. & TUMIN, A. 2011 High-speed boundary-layer instability: old terminology and a new framework. *AIAA J.* **49** (8), 1647–1657.
FEZER, A. & KLOKER, M. 2003 DNS of transition mechanisms at mach 6.8 – flat plate versus sharp cone. In *West East High Speed Flow Fields, 2002* (ed. D. E. Zeitoun, J. Periaux, J. A. Desideri & M. Marini), pp. 434–441. CIMNE.
GUO, P., HAO, J. & WEN, C. 2025 Transition reversal over a blunt plate at Mach 5. *J. Fluid Mech.* **1005**, A5.
GUO, P., HAO, J. & WEN, C.-Y. 2023 Interaction and breakdown induced by multiple optimal disturbances in hypersonic boundary layer. *J. Fluid Mech.* **974**, A50.
HAO, J., FAN, J., CAO, S. & WEN, C. 2022 Three-dimensionality of hypersonic laminar flow over a double cone. *J. Fluid Mech.* **935**, A8.
HAO, J. & WEN, C.-Y. 2021 Stabilization of a two-dimensional hypersonic boundary layer using a shallow cavity. *AIAA J.* **59** (2), 430–438.
HUANG, C., CAO, S., HAO, J., GUO, P. & WEN, C. 2025 Laminar-turbulent transition in a hypersonic compression ramp flow. *Phys. Fluids* **37** (3), 034110.
VAN INGEN, J. 2008 The en method for transition prediction. historical review of work at tu delft, In *38th Fluid Dynamics Conference and Exhibit*, American Institute of Aeronautics and Astronautics.
KARA, K., BALAKUMAR, P. & KANDIL, O.A. 2011 Effects of nose bluntness on hypersonic boundary-layer receptivity and stability over cones. *AIAA J.* **49** (12), 2593–2606.
LEKOUDIS, S.G. 1980 Stability of the boundary layer on a swept wing with wall cooling. *AIAA J.* **18** (9), 1029–1035.
LI, F., CHOUDHARI, M., CHANG, C.-L. & WHITE, J. 2010 Analysis of instabilities in non-axisymmetric hypersonic boundary layers over cones, In *10th AIAA/ASME Joint Thermophysics and Heat Transfer Conference*, American Institute of Aeronautics and Astronautics.
LIU, X., DONG, Y., LONG, T., ZHAO, R. & WEN, C.-Y. 2023 Stabilization mechanisms of various acoustic metasurfaces on the second mode in hypersonic boundary-layer flows. *Phys. Fluids* **35** (10), 104102.
LIU, Y., DONG, M. & WU, X. 2020 Generation of first mack modes in supersonic boundary layers by slow acoustic waves interacting with streamwise isolated wall roughness. *J. Fluid Mech.* **888**, A10.
LIU, Z. 2022 Cross-flow linear instability in compressible boundary layers over a flat plate. *Phys. Fluids* **34** (9), 094110.
LIU, Z. 2023 On the identification of cross-flow mode in three-dimensional boundary layers. *AIP Adv.* **13** (1), 015203.
LONG, T., DONG, Y., ZHAO, R. & WEN, C.-Y. 2021 Mechanism of stabilization of porous coatings on unstable supersonic mode in hypersonic boundary layers. *Phys. Fluids* **33** (5), 054105.
LU, J., UY, K.C.K., ZHAO, R. & WEN, C.-Y. 2025 Stabilization mechanisms of traveling crossflow mode in hypersonic swept wing flows. *AIAA J.* **63** (3), 1176–1190.
MA, Y. & ZHONG, X. 2003*a* Receptivity of a supersonic boundary layer over a flat plate. part 1. wave structures and interactions. *J. Fluid Mech.* **488**, 31–78.
MA, Y. & ZHONG, X. 2003*b* Receptivity of a supersonic boundary layer over a flat plate. part 2. receptivity to free-stream sound. *J. Fluid Mech.* **488**, 79–121.
MA, Y. & ZHONG, X. 2005 Receptivity of a supersonic boundary layer over a flat plate. part 3. effects of different types of free-stream disturbances. *J. Fluid Mech.* **532**, 63–109.
MACK, L.M. 1975 Linear stability theory and the problem of supersonic boundary- layer transition. *AIAA J.* **13** (3), 278–289.
MACK, L.M. 1984 *Boundary-Layer Linear Stability Theory*. AGARD Report No. 709
MALIK, M.R. 1990 Numerical methods for hypersonic boundary layer stability. *J. Comput. Phys.* **86** (2), 376–413.

https://doi.org/10.1017/jfm.2025.10708 Published online by Cambridge University Press

MALMUTH, N., FEDOROV, A., SHALAEV, V., COLE, J., HITES, M., WILLIAMS, D. & KHOKHLOV, A. 1998 Problems in high speed flow prediction relevant to control, In *2nd AIAA, Theoretical Fluid Mechanics Meeting*

MASAD, J.A. & ZURIGAT, Y.H. 1994 Effect of pressure gradient on first mode of instability in compressible boundary layers. *Phys. Fluids* **6** (12), 3945–3953.

MORKOVIN, M.V., RESHOTKO, E. & HERBERT, T. 1994 Transition in open flow systems: a reassessment. *Bull. Am. Phys. Soc.* **39** (9), 1–31.

MOYES, A., PAREDES, P., KOCIAN, T.S. & REED, H.L. 2016 Secondary instability analysis of crossflow on a hypersonic yawed straight circular cone, In *54th AIAA Aerospace Sciences Meeting*, American Institute of Aeronautics and Astronautics.

NIU, H., YI, S., HUO, J., ZHENG, W. & LIU, X. 2021 Experimental study on hypersonic crossflow instability over a swept flat plate by flow visualization. *Acta Mech. Sinica* **37**, 1395–1403.

NIU, H., YI, S., LIU, X. & FU, J. 2024 Experimental study of the early evolution of traveling crossflow instability on a 75° swept flat plate at Mach 6. *Phys. Fluids* **36** (12), 124133.

NIU, H., YI, S., LIU, X., HUO, J. & JIN, L. 2020 Experimental investigation of nose-tip bluntness effects on the hypersonic crossflow instability over a cone. *Int. J. Heat Fluid Flow* **86**, 108746.

NIU, H., YI, S., LIU, X., LU, X. & HE, L. 2019 Experimental study of crossflow instability over a delta flat plate at Mach 6. *AIAA J.* **57** (12), 5566–5574.

NIU, M. & SU, C. 2023 Receptivity and its influence on transition prediction of a hypersonic boundary layer over a small bluntness cone. *Phys. Fluids* **35** (3), 034109.

OWENS, L.R., BEELER, G.B., BALAKUMAR, P. & MCGUIRE, P. 2014 *Flow disturbance and surface roughness effects on cross-flow boundary-layer transition in supersonic flows*

PECK, M.M., GROOT, K.J. & REED, H.L. 2024 Boundary-layer instability on a highly swept fin on a cone at Mach 6. *J. Fluid Mech.* **987**, A13.

QIU, H., SHI, M., ZHU, Y. & LEE, C. 2024 Boundary layer transition of hypersonic flow over a delta wing. *J. Fluid Mech.* **980**, A57.

QUINTANILHA, H., PAREDES, P., HANIFI, A. & THEOFILIS, V. 2022 Transient growth analysis of hypersonic flow over an elliptic cone. *J. Fluid Mech.* **935**, A40.

REED, H.L. & SARIC, W.S. 1989 Stability of three-dimensional boundary layers. *Annu. Rev. Fluid Mech.* **21** (1989), 235–284.

REED, H.L., SARIC, W.S. & ARNAL, D. 1996 Linear stability theory applied to boundary layers. *Annu. Rev. Fluid Mech.* **28** (1996), 389–428.

REN, J. & FU, S. 2013 Nonlinear development of the multiple gortler modes in hypersonic boundary layer flows, In *43rd Fluid Dynamics Conference*, American Institute of Aeronautics and Astronautics.

SARIC, W.S. & REED, H.L. 2003 Crossflow instabilities–theory & technology, In *41st Aerospace Sciences Meeting and Exhibit*, American Institute of Aeronautics and Astronautics.

SARIC, W.S., REED, H.L. & KERSCHEN, E.J. 2002 Boundary-layer receptivity to freestream disturbances. *Annu. Rev. Fluid Mech.* **34**, 291–319.

SARIC, W.S., REED, H.L. & WHITE, E.B. 2003 Stability and transition of three-dimensional boundary layers. *Annu. Rev. Fluid Mech.* **35** (2003), 413–440.

SONG, R. & DONG, M. 2023 Linear instability of a supersonic boundary layer over a rotating cone. *J. Fluid Mech.* **955**, A31.

SONG, R., ZHAO, L. & HUANG, Z. 2020 Secondary instability of stationary görtler vortices originating from first/second mack mode. *Phys. Fluids* **32** (3), 034109.

STETSON, K. 1983 Nosetip bluntness effects on cone frustum boundary layer transition in hypersonic flow, In *16th Fluid and Plasmadynamics Conference*, American Institute of Aeronautics and Astronautics.

SU, C. & GENG, J. 2017 Interaction of weak free-stream disturbance with an oblique shock: validation of the shock-capturing method. *Appl. Math. Mechan.* **38**, 1601–1612.

SU, C., LI, G. & HAN, Y. 2024 Breakdown mechanisms induced by stationary crossflow vortices in hypersonic three-dimensional boundary layers. *Phys. Fluids* **36** (7), 074118.

UNNIKRISHNAN, S. & GAITONDE, D.V. 2019 Interactions between vortical, acoustic and thermal components during hypersonic transition. *J. Fluid Mech.* **868**, 611–647.

UY, K.C.K., HAO, J. & WEN, C.-Y. 2023*a* Coexistence of stationary görtler and crossflow instabilities in boundary layers. *Phys. Fluids* **35** (9), 094115.

UY, K.C.K., HAO, J. & WEN, C.-Y. 2023*b* Global and local analyses of the görtler instability in hypersonic flow. *Phys. Fluids* **35** (6), 064111.

WAN, B., CHEN, J., YUAN, X., HU, W. & TU, G. 2022 Three-dimensional receptivity of a blunt-cone boundary layer to incident slow acoustic waves. *AIAA J.* **60** (8), 4523–4531.

https://doi.org/10.1017/jfm.2025.10708 Published online by Cambridge University Press

WAN, B., TU, G., YUAN, X., CHEN, J. & ZHANG, Y. 2021 Identification of traveling crossflow waves under real hypersonic flight conditions. *Phys. Fluids* **33** (4), 044110.

WASSERMANN, P. & KLOKER, M. 2005 Transition mechanisms in a three-dimensional boundary-layer flow with pressure-gradient changeover. *J. Fluid Mech.* **530**, 265–293.

WHEATON, B.M., BERRIDGE, D.C., WOLF, T.D., ARAYA, D.B., STEVENS, R.T., MCGRATH, B.E., KEMP, B.L. & ADAMCZAK, D.W.2021 Final design of the boundary layer transition (bolt) flight experiment. *J. Spacecr. Rockets* **58** (1), 6–17.

XU, G., CHEN, J., LIU, G., DONG, S. & FU, S. 2019 The secondary instabilities of stationary cross-flow vortices in a Mach 6 swept wing flow. *J. Fluid Mech.* **873**, 914–941.

XU, G., LIU, G., CHEN, J. & FU, S. 2018 Role of freestream slow acoustic waves in a hypersonic three-dimensional boundary layer. *AIAA J.* **56** (9), 3570–3584.

ZHAO, R., WEN, C.-Y., LONG, T.H., TIAN, X.D., ZHOU, L. & WU, Y. 2019 Spatial direct numerical simulation of the hypersonic boundary-layer stabilization using porous coatings. *AIAA J.* **57** (11), 5061–5065.

ZHAO, R., WEN, C.-Y., TIAN, X.D., LONG, T.H. & YUAN, W. 2018 Numerical simulation of local wall heating and cooling effect on the stability of a hypersonic boundary layer. *Int. J. Heat Mass Tran.* **121**, 986–998.

ZHONG, X. & WANG, X. 2012 Direct numerical simulation on the receptivity, instability, and transition of hypersonic boundary layers. *Annu. Rev. Fluid Mech.* **44**, 527–561.

ZHU, W. & LEE, C. 2022 Perturbation decomposition over a flared cone with a wavy wall. In *AIAA AVIATION 2022 Forum*. American Institute of Aeronautics and Astronautics.

ZHU, Y., ZHU, W., GU, D., LEE, C. & SMITH, C.R. 2021 Characteristics of transition to turbulence over a Mach 6 flared cone. *Phys. Fluids* **33** (10), 101708.

ZURIGAT, Y.H., NAYFEH, A.H. & MASAD, J.A. 1992 Effect of pressure gradient on the stability of compressible boundary layers. *AIAA J.* **30** (9), 2204–2211.

https://doi.org/10.1017/jfm.2025.10708 Published online by Cambridge University Press